frontiers | Frontiers in Earth Science

TYPE Original Research
PUBLISHED 07 September 2022
DOI 10.3389/feart.2022.997008

OPEN ACCESS

EDITED BY
Qiangtai Huang,
Sun Yat-sen University, China

REVIEWED BY
Yunchuan Zeng,
China University of Geosciences, China
Sherif Farouk,
Egyptian Petroleum Research Institute, Egypt

*CORRESPONDENCE
Jérémie Aubineau,
jeremie.aubineau@umontpellier.fr

SPECIALTY SECTION
This article was submitted to Geochemistry, a section of the journal Frontiers in Earth Science

RECEIVED 18 July 2022
ACCEPTED 15 August 2022
PUBLISHED 07 September 2022

CITATION
Aubineau J, Parat F, Chi Fru E, El Bamiki R, Mauguin O, Baron F, Poujol M and Séranne M (2022), Geodynamic seawater-sediment porewater evolution of the east central Atlantic Paleogene ocean margin revealed by U-Pb dating of sedimentary phosphates. *Front. Earth Sci.* 10:997008. doi: 10.3389/feart.2022.997008

Geodynamic seawater-sediment porewater evolution of the east central Atlantic Paleogene ocean margin revealed by U-Pb dating of sedimentary phosphates

Jérémie Aubineau[1]*, Fleurice Parat[1], Ernest Chi Fru[2], Radouan El Bamiki[3], Olivia Mauguin[1], Fabien Baron[4], Marc Poujol[5] and Michel Séranne[1]

[1]Géosciences Montpellier, Université de Montpellier, CNRS UMR 5243, Montpellier, France, [2]Center of Geobiology and Geochemistry, School of Earth and Ocean Sciences, College of Physical Sciences and Engineering, Cardiff University, Cardiff, United Kingdom, [3]Mohammed VI Polytechnic University Geology and Sustainable Mining, Ben Guerir, Morocco, [4]IC2MP, Université de Poitiers, CNRS UMR 7285, Poitiers, France, [5]Univ Rennes, CNRS, Géosciences Rennes, UMR 6118, Rennes, France

Emerging evidence suggests that U-Pb and Lu-Hf ages of sedimentary apatite group minerals are often younger than their biostratigraphic ages. However, U-Pb dating of exquisitely preserved carbonate fluorapatite (CFA) is rare. The Upper Cretaceous/Paleogene marine sedimentary rocks of the Moroccan High Atlas host phosphate-rich sediments bracketed by calcareous nannofossil Zones (NP4-NP9) of late Danian to Thanetian age. Here, we use a laser-ablation inductively coupled plasma mass spectrometry (LA-ICP-MS) to decipher whether CFA minerals are suitable for U-Pb chronostratigraphy and whether they can reveal the sedimentary and seawater history from which they formed. U-Pb dating of the CFA grains yields ages of 42.9 $\pm$ 1.3 Ma (MSWD = 2.3) and 35.7 $\pm$ 2.8 Ma (MSWD = 1.3) from three distinct phosphate-rich beds, being >15 million years younger than the expected biostratigraphic age. Combined scanning electron microscopy, X-ray diffraction, and infrared spectroscopy analyses, associate the Mg-rich clay minerals sepiolite and palygorskite, with micro-CFA crystals, while LA-ICP-MS trace element, rare earth element, and yttrium content for primary CFA grains, collectively point to long-term early diagenetic adsorption from oxygenated seawater-dominated porewater fluids. Authigenic clay minerals display a seawater-like pattern, with negligible U concentrations suggesting limited clay mineral influence on U-Pb dating of the CFA crystals. Considering the absence of extensive post-depositional alteration, we propose that because of their large surface area, the µm-sized CFA crystallites facilitated real-time surface adsorption and desorption of elements and diffusion processes. These conditions generated long-term open system connection of sediments with overlying seawater, enabling continuous U-Pb exchange for 15–25 Myr after phosphate precipitation. The data suggest that system closure was potentially associated with sediment lithification and the Atlas orogeny, pointing to stable oxygenation of shallow marine waters along the eastern passive margin of the central Atlantic Ocean in the Paleogene.

KEYWORDS

carbonate fluorapatite, *in situ* U-Pb dating, Moroccan High Atlas, Paleogene, seawater signature

1 Introduction

Sedimentary apatite group minerals, hosted in marine phosphorus (P)-rich rocks (i.e., phosphorites), form in zones underlying strong upwelling currents (Föllmi, 1996). In such nutrient-rich environments, high biological productivity promotes an increase flux of sinking organic-bound P to the sediments. Multiple pathways lead to P burial; P is either organically bound if organic matter escapes remineralization or inorganically bound to Fe and Mn oxyhydroxides phases (Ruttenberg, 2003) in oxygenated environments, undergoing reductive dissolution in anoxic sediments to liberate P into porewaters. In contrast, P is dominantly preserved in authigenic apatite minerals, which are essentially fueled by 1) the release of organic-bound P during organic matter remineralization and 2) the hydrolysis of intracellular microbial polyphosphate reserves (Schulz and Schulz, 2005; Diaz et al., 2008). Authigenic P-rich phases precipitate from highly supersaturated porewater conditions containing dissolved phosphate of up to 400 $\mu mol.L^{-1}$ (Krajewski et al., 1994) immediately below the water-sediment interface.

High levels of supersaturation with respect to apatite, which controls nucleation rate, likely explain the large number of nano- to micro-metric crystals, being $>10^9$ per cm^3 in phosphate peloids (Krajewski et al., 1994). Pristine phosphate layers, containing <10 wt.% P_2O_5 (Pufahl and Groat, 2017) synsedimentary apatite minerals in varying proportions, accumulate during the initial step of phosphorite formation, as long as microbially mediated processes promote supersaturation with respect to apatite. In addition to biological stimulation of phosphate precipitation, *in situ* storm and bottom water currents may repeatedly winnow primary phosphate sediments, allowing phosphorites with >18 wt.% P_2O_5 (Glenn et al., 1994) to substantially accumulate (Föllmi, 1996; Filippelli, 2011; Pufahl and Groat, 2017). Depending on the strength, duration, and frequency of hydrodynamic agents, winnowing, reworking, and transport processes contribute to the enrichment of P in phosphorites (Pufahl and Groat, 2017). Thus, continental shelves and epeiric seas are preferred settings for the formation of large phosphate deposits due to prevailing hydrodynamic conditions that enable P enrichment (Pufahl and Groat, 2017).

The phosphogenic event that occurred in the South Tethyan province of North Africa and the Middle East, during the late Cretaceous and the Paleogene, led to the accumulation of the largest known phosphate deposit on Earth (Pufahl and Groat, 2017; Baioumy and Farouk, 2022, and references therein). Notably, Morocco hosts more than 70% of the world's phosphate reserves (Jasinski, 2020) in thin tabular beds mined in the western Meseta (Figure 1). Further deposits exist along the Moroccan High Atlas (MHA). Although mineralogical, sedimentological, sequence stratigraphy, and biostratigraphic investigations have been previously conducted on the MHA deposits (Gheerbrant et al., 1993; Daoudi, 2004; Tabuce et al., 2005; Knidiri et al., 2014; El Bamiki et al., 2020), they however remain largely unexplored.

Authigenic sedimentary apatite $[Ca_{10}(PO_4)_6(OH,F,Cl)_2]$ in marine environments is predominantly composed of carbonate fluorapatite (CFA)—$[Ca_{10-x-y}Na_xMg_y(PO_4)_{6-z}(CO_3)_z(F)_{0.4z}F_2]$ (McClellan, 1980). In equilibrium with seawater, CFA-hosted CO_3^{2-} content varies between 5 and 8 wt.% (Nathan, 1984). The accommodating chemical structure of apatite minerals allows easy incorporation of major and trace elements in the crystal lattice (e.g., Nathan, 1984). For example, a mean concentration of 120 ppm has been recorded for U in phosphorites (Altschuler, 1980), critical for U-Pb geochronology. Approaches for U-Pb dating of fossils, using biogenic hydroxyapatite, range from *in situ* and fission track techniques to solution methods (Sano and Terada, 1999; Romer, 2001; Sano et al., 2006; Balter et al., 2008; Jolivet et al., 2008; Fassett et al., 2011; Greene et al., 2018; Rochín-Bañaga et al., 2021).

Regardless of the dating techniques, it is worthy of mention that the U-Pb dates obtained from fossil bones and teeth are often younger and interpreted to reflect α-recoil effect and diagenetic alteration (e.g., Balter et al., 2008; Greene et al., 2018; Koenig et al., 2012; Romer, 2001). Controlled by both surface area and volume of the phosphate crystallites, α-recoil may generate a loss of daughter isotopes out of the apatite structure (Romer, 2001; Balter et al., 2008), yielding unconstrained, younger chronostratigraphic ages. Besides, diagenesis may be the locus of protracted interactions between fossil material and fluids, resetting the U-Pb radiometric system (Greene et al., 2018; Rochín-Bañaga et al., 2021).

The presence of significant amounts of common lead in the crystal lattice of apatite minerals is also a concern (Cochrane et al., 2014). Consequently, Phanerozoic sedimentary apatite may have low radiogenic Pb/common Pb ratios, leading to large age uncertainties. Furthermore, recent studies on *in situ* U-Pb dating of sedimentary phosphorites have barely constrained the chronostratigraphy of phosphate-bearing series (Molnár et al., 2018; Soares et al., 2019; O'Sullivan et al., 2021). Few of the studies cited above have integrated reliable screening techniques to identify diagenetic processes responsible for open system behavior in the samples analyzed by U-Pb method (e.g., Greene et al., 2018). Overall, linking U-Pb phosphate ages to the age of deposition is yet to be determined. The exquisite preservation of the Moroccan sedimentary apatite group minerals (e.g., Aubineau et al., 2022; Cosmidis et al., 2013;

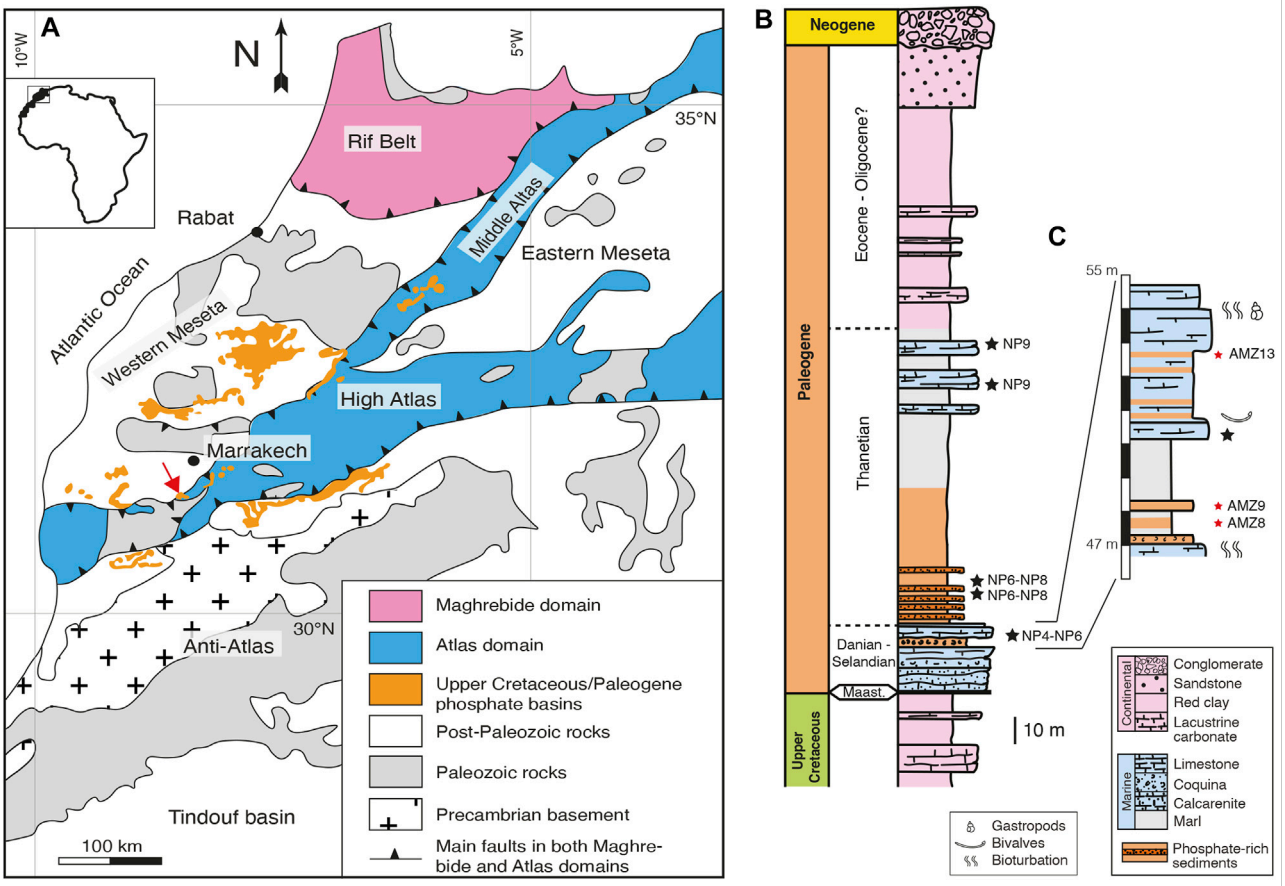

FIGURE 1
Geological map and lithostratigraphic column. **(A)** Simplified geological map and structural units of Morocco. The red arrow indicates the studied Amizmiz section, 31°12′09″N, 08°14′08″W. Geological map adopted from (Hollard et al., 1985) and the figure is modified from Aubineau et al. (2022). **(B)** Stratigraphic framework of the Amizmiz phosphate-bearing series. The figure is modified from El Bamiki et al. (2020). **(C)** Detailed lithostratigraphic column of the maximum flooding zone showing the sampled P-rich horizons. This interval results from a sedimentary condensation. Key nannofossil Zones are in black in b and c panels. NP: Paleogene Zonation.

Kocsis et al., 2014), offers a unique opportunity for distinguishing primary geochemical and geochronological signals from artefacts associated potential post-depositional changes, to gain better insights on their impact on U-Pb dating of phosphorites.

In this study, we explore *in situ* U-Pb CFA dating by laser ablation inductively coupled plasma mass spectrometry (LA-ICP-MS) to obtain precise chronostratigraphic ages for sedimentary phosphate rocks relative to their biostratigraphic sedimentary age. By constraining the precise chronostratigraphy of the Paleogene MHA phosphate sequence, we aimed to enhance stratigraphic correlations between the MHA and various phosphate deposits in Morocco and the South Tethyan province. The findings provide new insights on prevailing paleoenvironmental conditions, paleogeographic and geodynamic evolution of the eastern Atlantic passive margin on the Moroccan coast during the Paleogene.

2 Geological background of the Moroccan High Atlas

The Atlas domain, extending from the Atlantic coast to Tunisia, is weakly shortened, intracontinental fold belts that formed as a direct consequence of the Cenozoic African-Eurasian convergence (Michard et al., 2008). The Atlas structural zone, comprising the ENE-trending High Atlas and NE-trending Middle Atlas Mountain belts in Morocco, first developed as an intracontinental basin related to the Central Atlantic rifting during the Triassic (Frizon de Lamotte et al., 2008). The following thermal subsidence promoted the accumulation of km-thick, Mesozoic marine sedimentary successions (Ellouz et al., 2003). Then, the Atlas recorded a basin inversion possibly initiated in the late Cretaceous during the Alpine orogeny, which resulted in the lowering of thermal subsidence—thus of sediment deposition—as well as the

subsequent deformation and uplift of the Atlasic rocks during the Neogene (Ellouz et al., 2003; Frizon de Lamotte et al., 2008). The convergence-induced deformation remained weakly expressed by a slowing down of the post-rift thermal subsidence during the Paleocene, which allowed sediments to accumulate in a shallow platform within the MHA domain (El Bamiki et al., 2020). Although the timing of inversion events is uncertain, the deformation led to the formation of significant relief (Frizon de Lamotte et al., 2008; Frizon de Lamotte et al., 2009). Despite the continuous plate convergence, the deformation was discontinuous with two main tectonic episodes of shortening and uplift in the middle to late Eocene and late Miocene-Pliocene (Frizon de Lamotte et al., 2008; Frizon de Lamotte et al., 2009).

The MHA is notably composed of a wide variety of phosphate facies that have been related to both autocyclic, including wave and storm winnowing, and tectono-eustatic allocyclic processes (El Bamiki et al., 2020). The investigated Amizmiz section of the MHA consists of sedimentary rocks deposited during a second order relative sea-level cycle (El Bamiki et al., 2020). Most of the MHA sediments have been affected by km-size wave-length synclines (Frizon de Lamotte et al., 2008). The sedimentary series starts with Upper Cretaceous rocks that are dominated by continental sediments containing red fine-grained siliciclastic beds and yellowish lacustrine carbonates followed by a marine carbonate sequence. The subsequent subaerial exposure, caused by the large regression occurring during the late Cretaceous in the MHA domain, has karstified and eroded the Maastrichtian rocks in the Amizmiz area (Chellaï et al., 1995; El Bamiki et al., 2020). The Danian-Selandian rocks, deposited during a sea-level rise event, are dominated by shallow-water, bioclastic carbonates interbedded with thin layers of granular phosphates that mainly consist of winnowed and reworked phosphates in the Amizmiz area (El Bamiki et al., 2020). The overlying carbonates, deposited in the outer platform, are capped by a hardground surface, which is interpreted as reflecting the maximum bathymetry likely near the Selandian-Thanetian transition (Figure 1C; El Bamiki et al., 2020). This key marker is considered as a major stratigraphic surface that allows regional correlations in the MHA domain. In the wake of the maximum flooding, the phosphogenic window moved offshore of the outer carbonate platform in the western MHA domain (including the Amizmiz area). The net consequence is that large accumulations of pristine and winnowed phosphates were deposited. The phosphate sediments are typically crumbly. Overlying marls, marine carbonates, and continental sediments marked the progressive sea level fall in the MHA domain during the Eocene. Typical Lutetian *Thersitea* limestones overly the phosphate series in the western Meseta block and MHA domain (Boujo, 1976), but are eroded in the western MHA due to the following Atlasic, orogenic deformation (El Bamiki et al., 2020). The Neogene molassic sediments unconformably rest on the Upper Cretaceous/Paleogene sedimentary sequence.

Based on biostratigraphic data, the MHA phosphate series extends from late Cretaceous to Lutetian (Gheerbrant et al., 1993; Tabuce et al., 2005; and references therein). Notably, selachian fauna and planktonic foraminifera have helped to constrain the biostratigraphy of the phosphate sequence. Nonetheless, diachronous facies are likely in the MHA, which has raised concerns about these biostratigraphic ages (El Bamiki, 2020; El Bamiki et al., 2020). Moreover, organic carbon isotope compositions do not support the occurrence of Lutetian rocks in the phosphate series of the western Meseta domain (Yans et al., 2014). Nevertheless, a recent study of calcareous nannoflora allowed refining of the biostratigraphy in the lower to middle part of the Amizmiz sequence since some calcareous nannofossils provide reliable biohorizons (El Bamiki et al., 2020). Indeed, the Lowest Occurrences of *Toweius pertusus* (correlated to the foraminiferous NP4 Zone), *Fasciculithus tympaniformis* (NP5 Zone), *Heliolithus kleinpellii* (NP6 Zone), and *Discoaster multiradiatus* (NP9 Zone) collectively indicate a late Danian to Thanetian age of the main phosphate interval of the Amizmiz sedimentary sequence (El Bamiki et al., 2020).

In contrast, the upper part of the Amizmiz sequence is still poorly constrained. The sedimentation rate in the Amizmiz area can be approximately determined between the calcareous nannofossil biohorizons that are well correlated to the foraminiferous NP4 to NP9 zones. Although subject to relatively large uncertainties, a low sedimentation rate of ~20 m/Myr was estimated. In this study, we have targeted granular phosphate sediments for U-Pb dating due to their relevant stratigraphic positions, representing the maximum flooding event (Figures 1B,C; El Bamiki et al., 2020). Considering the nannoflora determination at this specific stratigraphic emplacement (Foraminiferous NP4-NP6 Zones), a late Danian to early Thanetian age is, thus, expected.

3 Samples and methods

3.1 Sampling and sample preparation

In the Amizmiz area (Figure 1A), three fresh, unweathered samples (designated as AMZ8, AMZ9, and AMZ13) were collected from the interval reflecting the regional-scale maximum bathymetry immediately above the hardground surface (Figures 1B,C; El Bamiki et al., 2020). Specifically, AMZ8 and AMZ9 samples are stratigraphically separated by less than 0.5 m, while AMZ13 is ~5 m stratigraphically above. Polished slab sections (from standard 2.5 cm-diameter mounts) for each sample were prepared for petrographic observations and *in situ* geochemical analyses using standard rock-polishing laboratory procedures at IC2MP, University of Poitiers. Portions of identical rock pieces were crushed and milled in agate mortar without using water for bulk mineralogical investigations.

3.2 Analytical methods

Scanning electron microscopy. Petrographic and mineralogical examination of carbon-coated, polished slab sections and rock slabs were performed using a FEI Quanta 200 FEG SEM equipped with an Oxford Instruments energy dispersive X-ray spectrometer (EDX) at MEA platform, University of Montpellier. Samples were imaged in secondary electron (SE) and backscattered electron (BSE) modes—operated under a low vacuum at an accelerating voltage of 10–15 kV, 1 nA beam current, and a working distance of 10 mm—to investigate the crystal size and morphology of minerals as well as textural relationships.

X-Ray Diffraction. Whole-rock powder and <2 µm clay mineral fraction of all samples were analyzed with XRD to characterize the mineralogy of MHA phosphorites. XRD patterns were acquired with a Bruker D8 ADVANCE diffractometer (CuKα radiation) operating at 40 kV and 40 mA at RRXG platform, University of Montpellier. The extraction protocol for the <2 µm clay fraction as well as XRD analytical conditions are provided in Supplementary Method. Bruker Eva software was used for indexing of peaks and the XRD patterns compared with reference data (Brindley and Brown, 1980).

Fourier transform infrared spectroscopy. The <2 µm fraction of AMZ8, AMZ9, and AMZ13 samples were further analyzed by the Fourier transform infrared (FTIR) spectroscopy at IC2MP, University of Poitiers. The study of OH-bending and OH-stretching vibration zones in middle infrared (MIR—400–4,000 cm^{-1}) is of deep interest for characterizing clay minerals (Farmer, 1974; Madejová et al., 2011). MIR spectra were acquired using a Nicolet iS50 FTIR spectrometer equipped with a potassium bromide (KBr) beamsplitter and a DTGS KBr detector. Spectra were obtained in transmission mode from KBr pellets; each spectrum is an accumulation of 100 scans acquired at 4 cm^{-1} resolution. KBr pellets are a mixture of 1 mg of sample and 149 mg of KBr that was pressed for 5 min at 8 kbar and dried overnight in an oven at 120°C.

In situ major and trace element compositions. Quantitative major and volatile element concentrations of phosphate minerals were measured using a CAMECA SX-100 electron microprobe equipped with wavelength dispersive spectrometers at MAGE platform, University of Montpellier. The analysis of all samples was performed to geochemically characterize the phosphate composition and determine Ca abundances for LA-ICP-MS internal standardization. Electron probe microanalyses (EPMA) were performed with an acceleration voltage of 15 kV, 20 nA beam current, and a ~1 µm focused beam. Additional information on the EPMA methodology and detection limits are detailed in Supplementary Method and Supplementary Table S1. Furthermore, trace element concentrations were determined by LA-ICP-MS using a ThermoFinnigan Element XR ICP-MS coupled with a Geolas platform housing a 193 nm Compex 102 laser from LambdaPhysik at AETE platform (OSU-OREME), University of Montpellier. The laser beam was characterized by a 6 $J.cm^{-2}$ energy density, 6 Hz repetition rate, and 50 µm spot size. LA-ICP-MS analyses were calibrated with NIST standard reference materiel 612 values (Pearce et al., 1997). BIR-1G standard was used as external standard. Data processing and reduction are detailed in Supplementary Method. LA-ICP-MS standard values and their corresponding standard deviation (1σ) and detection

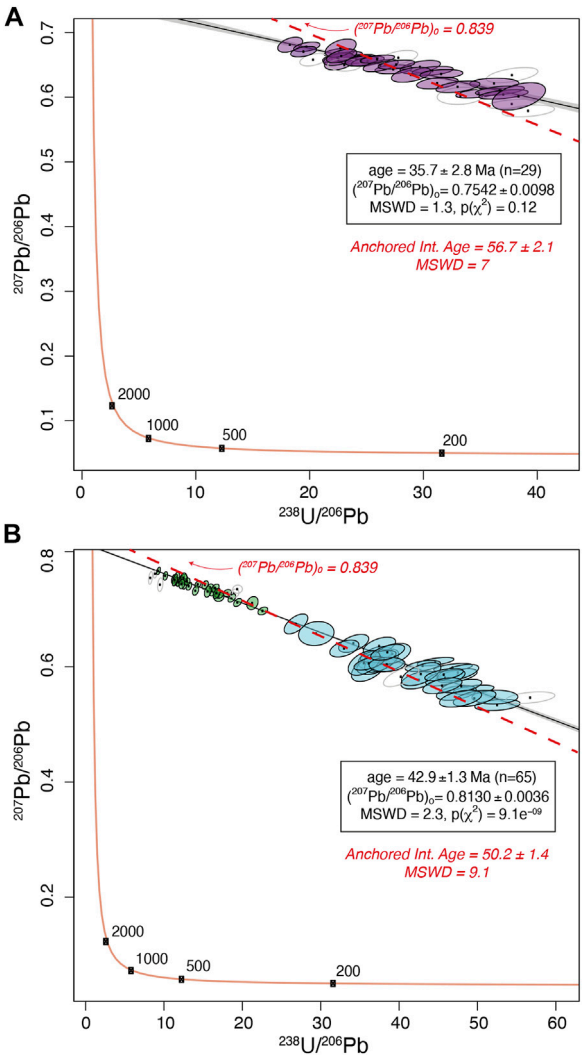

FIGURE 2
Tera-Wasserburg concordia diagrams for U-Pb dating of CFA in the Moroccan High Atlas. **(A)** AMZ13 sample. **(B)** AMZ9 (green) and AMZ8 (blue) samples. Black lines represent unanchored discordias. Following the Pb model of Stacey and Kramers (1975), red dashed-lines represent anchored discordias that were calculated with an initial $(^{207}Pb/^{206}Pb)_0$ ratio of 0.839, corresponding to an emplacement age of ~60 Myr. Unfilled ellipses were excluded from age calculations. Ellipses and errors are reported at 2σ. MSWD: Mean Squared Weighted deviation.

limits are reported in Supplementary Table S2. LA-ICP-MS measurements were realized close to the EPMA areas to carefully screen any possible weathering and diagenetic influences, using rare earth elements and yttrium (REEY) geochemistry (Supplementary Method for methods of calculation).

U-Pb analyses. AMZ8, AMZ9, and AMZ13 samples were investigated for U-Pb geochronology on sedimentary apatite, using a LA-ICP-MS at the GeOHeLiS analytical platform, University of Rennes. Detailed instrumental conditions of the U-Pb LA-ICP-MS analyses and analytical set-up are provided in Supplementary Table S3. Our data are originally uncorrected for common Pb due to the isobaric interference between ^{204}Pb and ^{204}Hg. More information about the analytical protocol can be found in Pochon et al. (2016). The primary apatite reference material used was Madagascar apatite standard (Chew et al., 2014; 473.5 ± 0.7 Ma), while Durango (McDowell et al., 2005; 31.44 ± 0.18 Ma) and McClure (Schoene and Bowring, 2006; 523.51 ± 2.09 Ma) apatite reference materials were analyzed as unknown to control reproducibility. The latter yielded ^{207}Pb-corrected ages of 31.8 ± 0.3 Ma (n = 36) and 528.9 ± 3.3 Ma (n = 30), respectively (Supplementary Figure S1). Isotopic data of apatite standards, at 2σ confidence, are presented in Supplementary Table S4. Finally, petrographic images of studied samples are provided with all positions of *in situ* geochemical analyses (Supplementary Figure S2).

4 Sedimentary phosphate dating

We analyzed up to 30 phosphate grains for each of three MHA phosphorites. All U-Pb LA-ICP-MS data with corresponding 2σ uncertainties are reported in Supplementary Table S5 and plotted in Tera-Wasserburg diagrams using IsoplotR (Figure 2) (Vermeesch, 2018).

Mean U concentrations of the investigated samples, 58.6 ± 5.7 ppm (1σ, n = 15), 45.1 ± 6.8 ppm (n = 12), 42.7 ± 9.6 ppm (n = 13) for AMZ8, AMZ9, and AMZ13, respectively (Supplementary Table S6), fall within the acceptable range suitable for U-Pb dating. A total of 108 U-Pb LA-ICP-MS measurements were conducted, all producing discordant results. The samples equally displayed a high proportion of common Pb with ^{207}Pb/^{206}Pb values ranging from 0.534 to 0.674, 0.697 to 0.766, and 0.579 to 0.681 for AMZ8, AMZ9, and AMZ13, respectively (Figure 2). Isotopic data for AMZ8 and AMZ9 plot along the same discordia, with a lower intercept date of 42.9 ± 1.3 Ma (MSWD = 2.3) (Figure 2B) and 35.7 ± 2.8 Ma (MSWD = 1.3) for AMZ13 (Figure 2A). Using an initial ^{207}Pb/^{206}Pb composition estimated from the crustal Pb evolution model of Stacey and Kramers (1975), a common Pb correction on the Tera-Wasserburg diagrams was also applied as significant amounts of common Pb are hosted in the MHA CFA. The modelled common Pb value was therefore anchored to a $(^{207}Pb/^{206}Pb)_0$ value of 0.839 (upper intercept) calculated for an age of 60 Ma (i.e., the expected age for the deposition of MHA phosphorites). The resulting lower intercepts of anchored discordia dates of 50.2 ± 1.4 Ma (MSWD = 9.1) and 56.7 ± 2.1 Ma (MSWD = 7) were inferred for the AMZ8-AMZ9 and AMZ13 samples, respectively. The MSWD of these anchored discordias are rather large (>7), which makes the corresponding lower intercept dates unreliable. Importantly, the U-Pb isotope values of phosphate grains show well-defined isochrons with a lack of significant scattering (Figure 2), suggesting that age constraints are robust. Nonetheless, the U-Pb dates are up to >15 Myr younger than the known late Danian to early Thanetian biostratigraphic ages (Foraminiferous NP4-NP6 Zones; Figure 1; El Bamiki et al., 2020). It is possible that the U-Pb ages of the MHA phosphorites are not related to the age of phosphate precipitation. We therefore screened for potential environmental controls and post-depositional processes that may have influenced the validity of the U-Pb dates.

5 Weathering and diagenetic screening

5.1 Nanoscale intergrowths between clay and phosphate minerals

Petrographic observations usually allow a better understanding of rock texture and mineral paragenetic relationships with indications of diagenetic alterations, if any (e.g., Middleton et al., 2003). SEM examinations reveal that the MHA phosphorites commonly consist of rounded and elongated phosphate peloids embedded in a clayey matrix (Figures 3A–C, 4A). Concavo-convex contacts between phosphate grains suggest a weak to moderate mechanical compaction (Figures 3A,B). Clay minerals are squeezed into pore between phosphate grains, which suggests that their formation predates compaction (Figure 3B). Rhombohedral dolomite, euhedral calcite crystals, and minor detrital grains, including quartz and titanium oxides, also compose the matrix (Figure 3C). In contrast to calcite, dolomite crystals exhibit partial dissolution features (Figure 3C). Finally, the interior of broken peloids shows high porosity occasionally filled by clay particles, as suggested by the presence of O, Si, Mg, and Al elements through EDX analysis (Figure 3D; Supplementary Figure S3A).

The P-rich grains measure 365 ± 147 μm (1σ, n = 50) in size without irregular and discontinuous phosphate layers, suggesting poorly transported phosphorites and supporting their accumulation by an *in situ* winnowing environment (Pufahl and Grimm, 2003). Micrometric sphere-like crystallites with an average diameter of 0.53 ± 0.17 μm (1σ, n = 40) form the peloids (Figures 4B–D). Numerous pits are observed at the peloid surface, draped by a clay coating. Moreover, the clay matrix is characterized by unoriented phyllosilicate fibers and fan-shaped

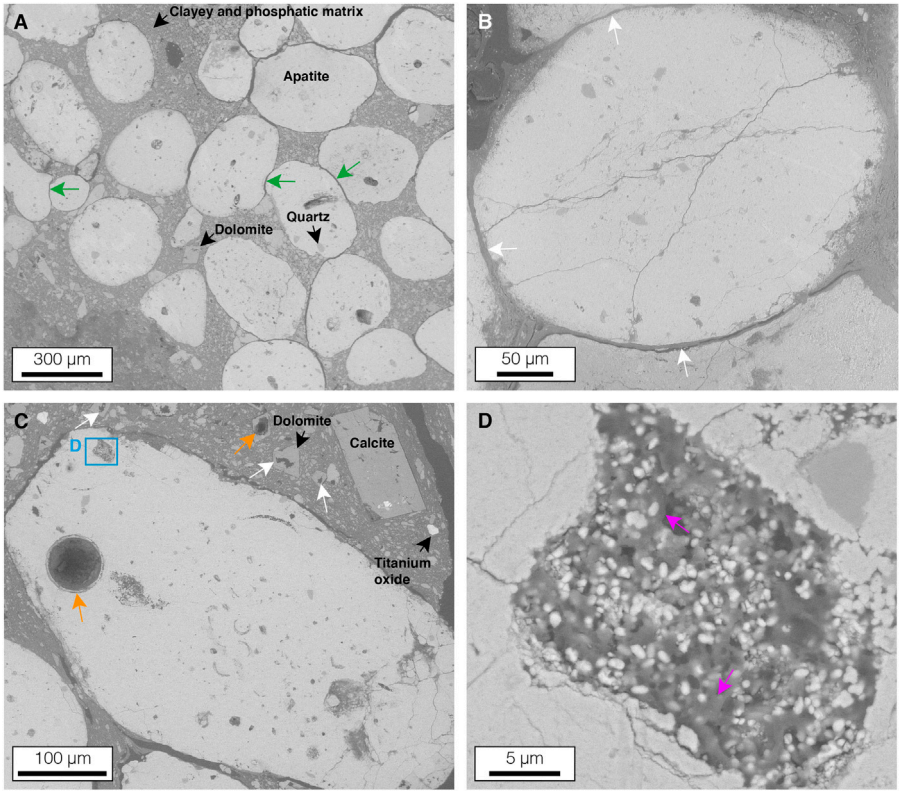

FIGURE 3
SEM images in back-scattered electron mode of Amizmiz phosphorites from the Moroccan High Atlas. **(A)** The phosphate grains are embedded in a dominantly clayey matrix in association with carbonate minerals. The P-rich grains experienced a weak to moderate degree of compaction as shown by the concavo-convex grain contacts (green arrows). **(B)** The clayey matrix is squeezed between phosphate peloids due to mechanical compaction (arrows). **(C)** Large and irregular phosphate peloid with numerous inclusions of quartz and fragmented shells. Orange and white arrows indicate traces left by *in situ* geochemical measurements and secondary dissolution features of rhombohedral dolomite, respectively. **(D)** Close up of image **(C)**. Micrometric phosphate crystallites surrounded by a thin clayey structure within the peloid (arrows).

fiber bundles (Figures 4B,E,F), which are typical morphologies of sepiolite [$Si_{12}O_{30}Mg_8(OH)_4(OH_2)_4{\cdot}8H_2O$] and palygorskite [$Si_8O_{20}(Mg_2Al_2)(OH)_2(OH_2)_4{\cdot}4H_2O$] minerals (Knidiri et al., 2014; Kadir et al., 2016). Fiber particles have a micrometric length and a width of less than 0.2 µm (Figures 4E,F). The EDX spectrum of fibers mainly consists of Si and Mg with little Al and Fe, consistent with the suggested presence of Mg-rich clay minerals such as sepiolite and palygorskite (Supplementary Figure S3B). Considering that both fibrous minerals can appear together at the crystallite scale, morphological distinctions between sepiolite and palygorskite are, however, difficult at this magnification. Platy particles are also recognized in the matrix, which could be indicative of smectite-like swelling clays (Figure 4F). The association of smectite, sepiolite, and palygorskite has already been observed (Daoudi et al., 2009; Suárez and García-Romero, 2013; Knidiri et al., 2014; Kadir et al., 2016). The apparent clay coating texture on the MHA phosphate peloids and as pore filling point to authigenic rather than detrital origin, postdating phosphogenesis. Although the U-Pb measurements were performed on large phosphate peloids, our microscopic observations reveal that the U-Pb dates may also incorporate a mixed signal, caused by the unavoidable presence of nm-sized phyllosilicates that were introduced through highly porous spaces that existed between the phosphate crystallites.

5.2 Weak burial diagenesis

The CO_3^{2-} content of CO_3^{2-}-rich fluorapatite may also serve as a good indicator of post-depositional alteration (McArthur, 1978; McClellan, 1980; McClellan and Van Kauwenbergh, 1991). Besides, the assemblage of clay minerals in sedimentary deposits, is mainly used as proxies for fluid-rock interactions, paleoclimatic, paleoenvironmental, and thermal diagenetic events in sedimentary rocks of Earth's surface (Meunier, 2005; Wilson, 2013; Aubineau et al., 2021). Therefore, the integrated study of phosphate and clay mineralogy should provide pertinent

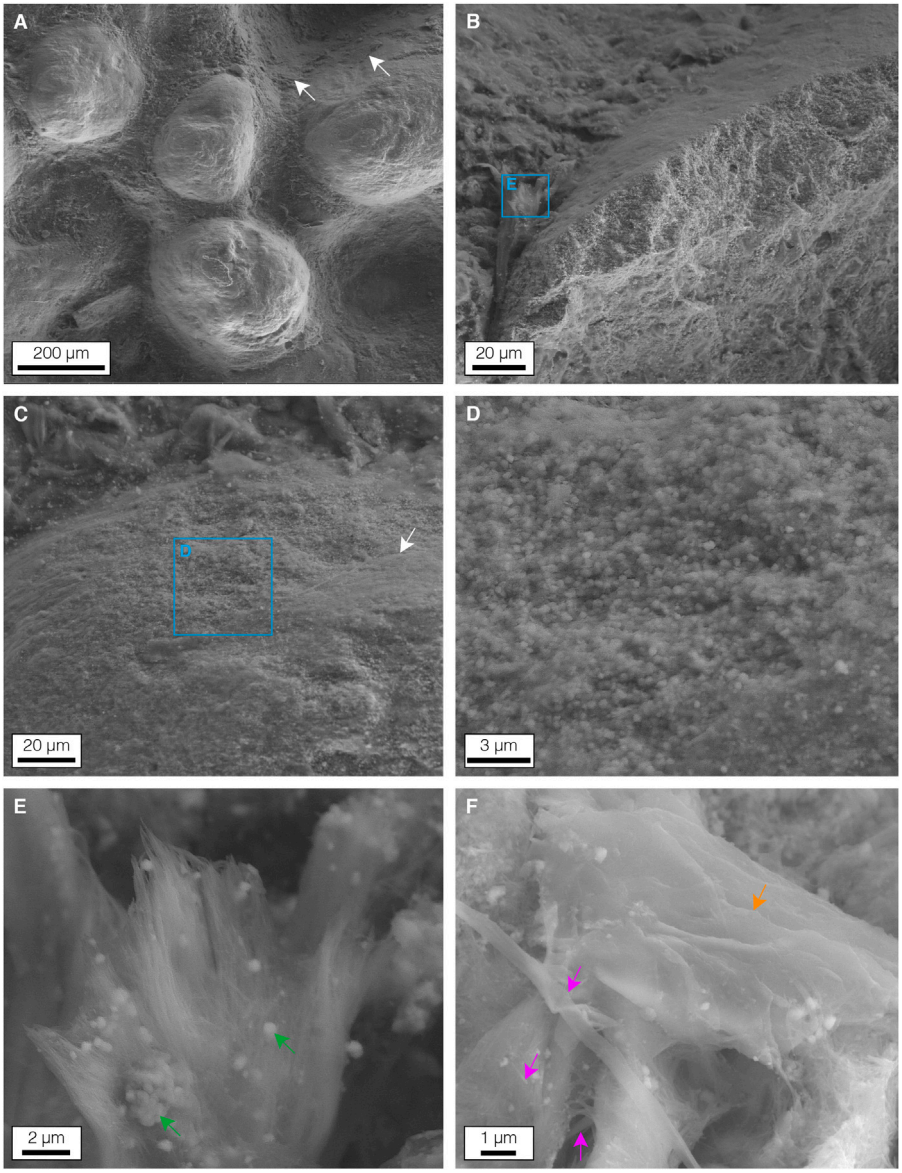

FIGURE 4
SEM images in secondary electron mode of Amizmiz phosphorites from the Moroccan High Atlas. **(A)** Rounded to slightly elongated phosphate peloids enclosed in a finely laminated matrix (arrows). **(B)** Broken phosphate grain that consists of densely packed crystallites. **(C)** The peloid surface is splotchy and occasionally draped by clayey layers (arrow). **(D)** Close up of image **(C)**. High density of sphere-like phosphate crystallites intertwined with a clayey material filling the porosity. **(E)** Close up of image **(B)**. Fan-shaped fiber bundle typical of sepiolite/palygorskite clay minerals. Arrows show the sphere-like phosphate crystallites. **(F)** Nm- to µm-long sepiolite/palygorskite fibers (purple arrows) in association with platy phyllosilicates (orange arrow) like smectite minerals.

information on secondary weathering and diagenetic history of the Amizmiz rock sequence.

Bulk XRD mineralogical data show that the MHA phosphorites are mainly composed of CFA as the main phosphate mineral with varying clay minerals, quartz, calcite, and dolomite occurring in relatively small proportions (Supplementary Figure S4A). The (211) and (300) strong reflections of CFA are shifted towards higher 2°θ values compared to fluorapatite, which suggests substitutions of CO_3^{2-} for PO_4^{3-} within CFA (LeGeros et al., 1967; Jahnke, 1984). Using an empirical equation between the CO_3^{2-} concentration and the difference in °2θ (Δ2θ) of the (004) and (410) CFA reflections (Schuffert et al., 1990), the estimated CO_3^{2-} contents of CFA in the MHA phosphate deposits (n = 3) range from 8.03 to 8.36 wt.% ± 0.5 % (Table 1; Supplementary Figure S4B). It should be noted that the presence of dolomite does not

TABLE 1 XRD reflections and estimated CO_3^{2-} contents (wt.%) for the Amizmiz phosphorites. The carbonate concentration (wt.%) in CFA grains is calculated as $10.643x^2 - 52.512x + 56.986$ where x stands for $\Delta 2\theta_{(004-410)}$ (Schuffert et al., 1990).

Area	Height (m)	Sample	(410) Å	(004) Å	(410) °2θ	(004) °2θ	Δ2θ	CO_3^{2-} content
Amizmiz	52.8	AMZ13	1.76150	1.72321	51.863	53.105	1.241	8.20
	48.1	AMZ9	1.76215	1.72363	51.843	53.091	1.248	8.03
	47.6	AMZ8	1.76180	1.72368	51.854	53.089	1.235	8.36

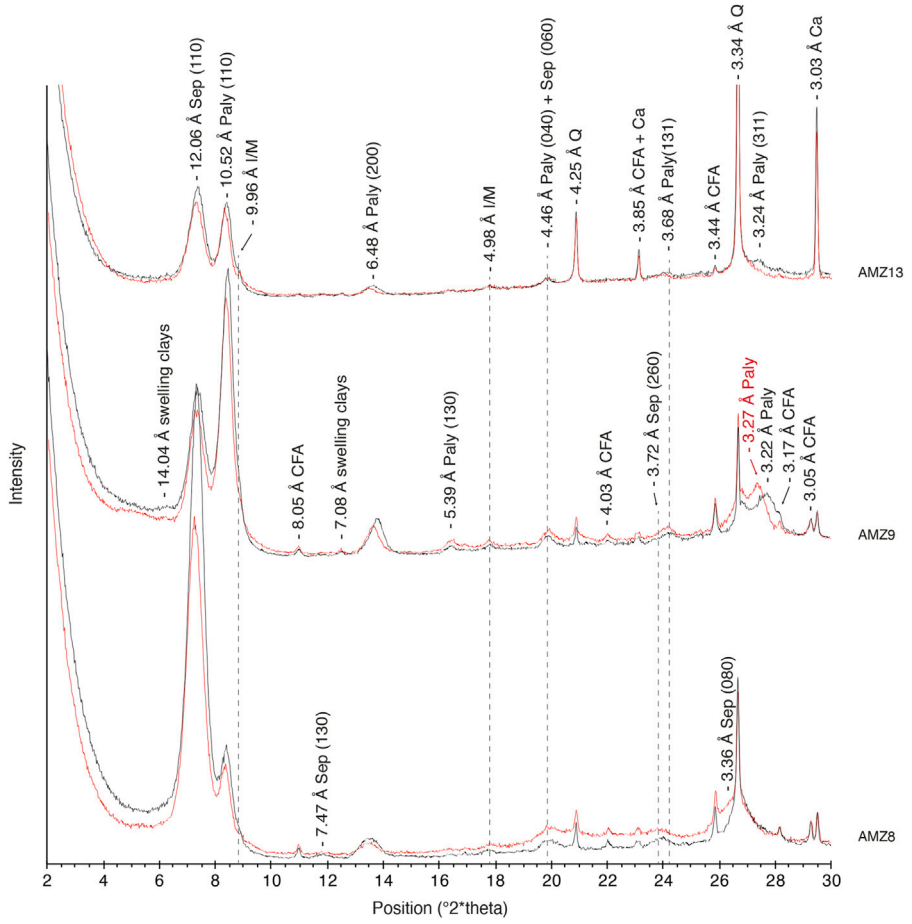

FIGURE 5
XRD patterns of the <2 µm clay fraction of Amizmiz phosphorites. Oriented preparations after airdrying (black lines) and glycolation (red lines). Sepiolite (Sep); Palygorskite (Paly) illite/mica (I/M); quartz (Q); carbonate fluorapatite (CFA); calcite (Ca).

overestimate the CO_3^{2-} concentration of CFA (Aubineau et al., 2022). The clay-sized fraction of oriented preparations consists mainly of trioctahedral sepiolite and dioctahedral palygorskite clays (Figure 5). Sepiolite is defined by peaks at ~12.06 Å, 7.47 Å, 4.46 Å, 3.72 Å, and 3.36 Å, while palygorskite is characterized by a strong peak at ~10.52 Å as well as minor reflections at ~6.48 Å, 5.39 Å, 4.46 Å, 3.68 Å, and ~3.24 Å (Knidiri et al., 2014; Kadir et al., 2016). The position of their main reflections slightly varies from one sample to another, which is explained by heterogeneous Mg and Al contents in these minerals (Suárez et al., 2007; Suárez and García-Romero, 2013). Both sepiolite and palygorskite slightly expand to 0.2 and 0.1 Å, respectively, after saturation with ethylene glycol (Figure 5), which results from minute internal penetration of ethylene glycol into the channel of

these fibrous clays (Wilson, 2013). In addition, swelling clays and mica are occasionally present in small amount.

FTIR analyses of the MHA clay-sized fraction were performed to further characterize the clay mineralogy in the OH-bending and OH-stretching vibration regions (Supplementary Figure S5). The OH bending bands, occurring at 443, 651 and 696 cm^{-1}, indicative of lattice, δSi–O, and δMg_3–OH vibrations, respectively (Supplementary Figure S5A), reveal the presence of trioctahedral Mg clay minerals. On the other hand, the 512 cm^{-1} absorption band is attributed to δSi–O–^{IV}Al bending vibrations of dioctahedral Al clay minerals. Other spectra bands in the OH-bending region are dominated by the signature of phosphate minerals (568, 578, and 604 cm^{-1}), dolomite (712 cm^{-1}), and quartz (776 and 797 cm^{-1}) (Farmer, 1974; Comodi and Liu, 2000; Madejová et al., 2011). Furthermore, the OH stretching region shows one trioctahedral Mg clay mineral absorption band at 3,680 cm^{-1}, reflecting the νMg_3–OH vibrations, while two dioctahedral Al phyllosilicates bands at 3,613 and 3,621 cm^{-1} are due to νAl_2–OH vibrations (Supplementary Figure S5B).

The OH stretching band at ~3,560 cm^{-1} is attributed to νFe^{3+}Mg–OH or $\nu 2Fe^{3+}$–OH vibrations (Wilson, 2013). A slight shift of this band towards higher or lower frequencies may represent substitutions of Fe^{2+} for Mg in octahedral layers. Finally, the ~3,400 cm^{-1} broad band is related to the presence of bound water molecules in phyllosilicates (Wilson, 2013). Considering the small contributions of swelling clays and micas in the MHA phosphorites (Figure 5), vibrational bands of trioctahedral clay structure, more intense in AMZ8 spectrum, are mainly related to sepiolite (Mg-rich clay), while dioctahedral clay structure vibrational bands are diagnostic of palygorskite Al- and Mg-rich clay. FTIR analyses point to an absence of distinguished features of other clay minerals, supporting XRD data.

Primary CFA are defined by a relatively uniform CO_3^{2-} content, from 5 to 8 wt.%, reflecting the equilibrium with seawater or porewaters in connection with the overlying water column (Nathan, 1984). Low-temperature alteration, including weathering and diagenesis can lead to a significant CFA decarbonation through time, resulting from the metastability of CFA with respect to fluorapatite (Chien and Black, 1976; McClellan and Van Kauwenbergh, 1991). Unaltered CFA from the Gantour basin, about 100 km northward of the studied section, contain on average 7.42 ± 0.74 wt.% (1σ, n = 5) of CO_3^{2-} (Aubineau et al., 2022), which is similar to our measured CO_3^{2-} concentrations. Moreover, the XRD patterns and MIR spectra, together with SEM observations revealed the occurrence of both sepiolite and palygorskite in the MHA phosphorites. Sepiolite and palygorskite authigenesis typically occur in lacustrine and lagoonal environments under semi-arid/arid and evaporitic climatic conditions (Singer and Galan, 1984). The formation of sepiolite-palygorskite has also been recorded in coastal marine environments during late Cretaceous to Eocene times since the climate was warm (Wilson, 2013). Specifically, these fibrous clay minerals precipitate from alkaline pH 8 to 9 and from saline waters with high Si and Mg activities (Weaver and Beck, 1977). Besides, increasing burial temperature (>100°C) during diagenesis leads to transformation of sepiolite-palygorskite (Weaver and Beck, 1977). Depending on the morphology of fibers, sepiolite and palygorskite may crystallize by direct chemical precipitation from evaporitic lake or supersaturated interstitial waters and by dissolution/recrystallization processes of a smectitic precursor (Wilson, 2013; Knidiri et al., 2014).

The absence of widespread swelling clays and fibrous sepiolite-palygorskite growing on platy smectite suggests that the transformation of smectite to sepiolite-palygorskite was not the dominant mechanism in the Amizmiz phosphorites. Secondary partial dissolution of rhombohedric dolomitic crystals could have resulted from changes in physiochemical conditions of the environments, which would have favored subsequent sepiolite and palygorskite precipitation (Weaver and Beck, 1977; Akbulut and Kadir, 2003; Kadir et al., 2017). Considering the low amount of dolomite in the Amizmiz samples, it is unlikely that all sepiolite-palygorskite-hosted Mg derived from the dissolution of dolomite. Rather, sepiolite and palygorskite chemically precipitated under supersaturated conditions. Importantly, the preservation of sepiolite and palygorskite, together with unaltered CFA, suggest that the Amizmiz sediments have undergone negligible diagenetic modifications.

5.3 Seawater-influenced chemical environments

While the composition of the major elements of phosphate grains has been used to document the chemistry of overlying seawater and porewaters of sediments (Glenn et al., 1988; Jarvis et al., 1994; Pufahl and Grimm, 2003; Arning et al., 2009; Aubineau et al., 2022), REEY in phosphate sediments are reliable tracers of paleo-oceanographic environments and post-depositional processes that affect sedimentary rock sequences (e.g., Reynard et al., 1999; Morad and Felitsyn, 2001; Shields and Stille, 2001; Kidder et al., 2003; Garnit et al., 2012; Kocsis et al., 2016; Lumiste et al., 2019; Ahmad et al., 2020; Yang et al., 2021; Baioumy and Farouk, 2022; Valetich et al., 2022). We studied the major and trace element geochemistry of the phosphate and clay minerals to decipher whether elemental composition could ascertain the chemical environments from which they formed.

5.3.1 Major element distribution in CFA peloids

The EPMA of the CFA grains show mixed chemical compositions between apatite and Mg-rich and Mg-poor clay minerals (Supplementary Figure S6; Supplementary Table S1).

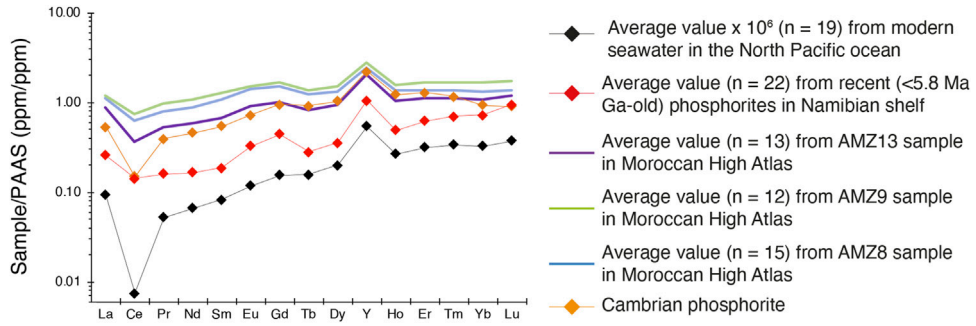

FIGURE 6
Average PAAS-normalized REEY values of Amizmiz phosphorites from the Moroccan High Atlas (blue, green, and purple lines) compared with the average $REEY_{SN}$ spectrum of modern seawater (Alibo and Nozaki, 1999; black line), recent marine phosphorites (Lumiste et al., 2019; red line) and unaltered Cambrian phosphorite (IX-25, Shields and Stille, 2001; orange line). Seawater-like patterns in the Amizmiz samples are preserved with no MREE arching. Data from this study and Lumiste et al. (2019) were collected by LA-ICP-MS, while Shields and Stille's (2001) and Alibo and Nozaki's (1999) values come from bulk ICP-MS analyses. PAAS values are from Taylor and McLennan (1985).

Consequently, the average structural formulae of CFA cannot be calculated. Quantitative major element mapping of the MHA phosphorites reveal homogeneous Ca and P—and thus CO_3^{2-} composition of the CFA grains (Supplementary Figure S7). Accessory minerals like sulfides are absent within the CFA peloids. Combined, these observations indicate uniform rate of organic matter remineralization and stable organic carbon export at the water-sediment interface during phosphogenesis, resulting in negligible local increase in alkalinity and porewater anoxic/sulfidic conditions (Pufahl and Grimm, 2003; Arning et al., 2009; Aubineau et al., 2022).

5.3.2 REEY distribution in CFA grains

The LA-ICP-MS results and corresponding REEY-based proxies are presented in Supplementary Table S6. Compared to unaltered modern and ancient phosphorites, PAAS-normalized REEY patterns (hereafter referred to as $REEY_{SN}$) of MHA CFA are relatively similar (Figure 6; Supplementary Figure S8). The uniformity of all $REEY_{SN}$ patterns hints uptake of REEY from a geochemically uniform fluid. On the other hand, the MHA P-rich peloids are characterized by higher $REEY_{SN}$ contents than the recent Namibian apatite grains and Cambrian phosphorites. Further, $REEY_{SN}$ distribution in the MHA CFA grains are depleted in $LREE_{SN}$ relative to $HREE_{SN}$, they contain negative Ce anomalies, slight positive Gd anomalies, and high Y/Ho ratios, characteristics pronounced for a seawater source (Bolhar et al., 2004; and references therein).

None of the CFA grains display the "bell-shaped" MREE enrichment pattern (Figure 6; Supplementary Figure S8) diagnostic of intensive diagenetic REE scavenging (Shields and Stille, 2001). Similarly, the mean bell-shaped index, which assesses the degree of middle REE enrichment, is 1.12 ± 0.09, 1.08 ± 0.05, and 0.99 ± 0.04 for the AMZ8, AMZ9, and AMZ13 samples, respectively, consistent with the absence of strong diagenetic influence. Moreover, $(Sm/Yb)_{SN}$ and $(Sm/Pr)_{SN}$ ratios plot on the HREE enriched field (Figure 7A). Specifically, $(Sm/Yb)_{SN}$ averaged 0.79 ± 0.12, 0.77 ± 0.07, and 0.62 ± 0.05 for the AMZ8, AMZ9, and AMZ13, respectively, with corresponding averaged $(Sm/Pr)_{SN}$ ratios of 1.33 ± 0.09, 1.29 ± 0.06, and 1.28 ± 0.04, respectively. The $(Ce/Ce^*)_{SN}$ vs. $(Pr/Pr^*)_{SN}$ diagram shows that the samples display true negative Ce anomalies (Figure 7B), taken to reflect oxygenated seawater and porewater conditions.

A positive La anomaly, causing apparent negative Ce anomaly, is sometimes observed in a few AMZ8 and AMZ9 grains. Importantly, the lack of strong correlations between $(Ce/Ce^*)_{SN}$ and $(Dy/Sm)_{SN}$ in the MHA samples indicates that the negative Ce anomalies were not controlled by diagenetic fluids (Figure 7C) (Shields and Stille, 2001). However, a $(La/Yb)_{SN}$ vs. $(La/Sm)_{SN}$ plot suggests a weak or 'early' diagenetic adsorption of REE by the CFA grains cannot be ruled out (Figure 7D; Reynard et al., 1999). $(La/Yb)_{SN}$ ratios, ranging from 0.63 to 0.98, are slightly higher than those of modern seawater, while $(La/Sm)_{SN}$ ratios, between 0.85 and 1.57, are similar (Shields and Stille, 2001). The MHA CFA peloids display uniform and slightly positive Eu and Gd anomalies with $(Eu/Eu^*)_{SN}$ values of 1.23 ± 0.04, 1.18 ± 0.05, and 1.25 ± 0.06 as well as $(Gd/Gd^*)_{SN}$ values of 1.30 ± 0.03, 1.26 ± 0.04, and 1.31 ± 0.04 for the AMZ8, AMZ9 and AMZ13 samples, respectively (Figure 6; Supplementary Figure S8; Supplementary Table S6). Strong positive Eu anomalies (>2), usually promoted by high-temperature hydrothermal fluxes (>200°C) (Bolhar et al., 2004; Planavsky et al., 2010), are not observed in our samples. A Gd enrichment relative to the neighboring Eu and Tb rather implies a seawater origin (De Baar et al., 1985). On the other hand, Gd enrichment could simply reveal differences in surface complexation compared with Eu and Tb (Kim et al., 1991). The average Y/Ho ratios of the AMZ8, AMZ9, and AMZ13 samples are 49.56 ± 3.51, 49.18 ± 3.37, and 54.98 ± 3.54, respectively

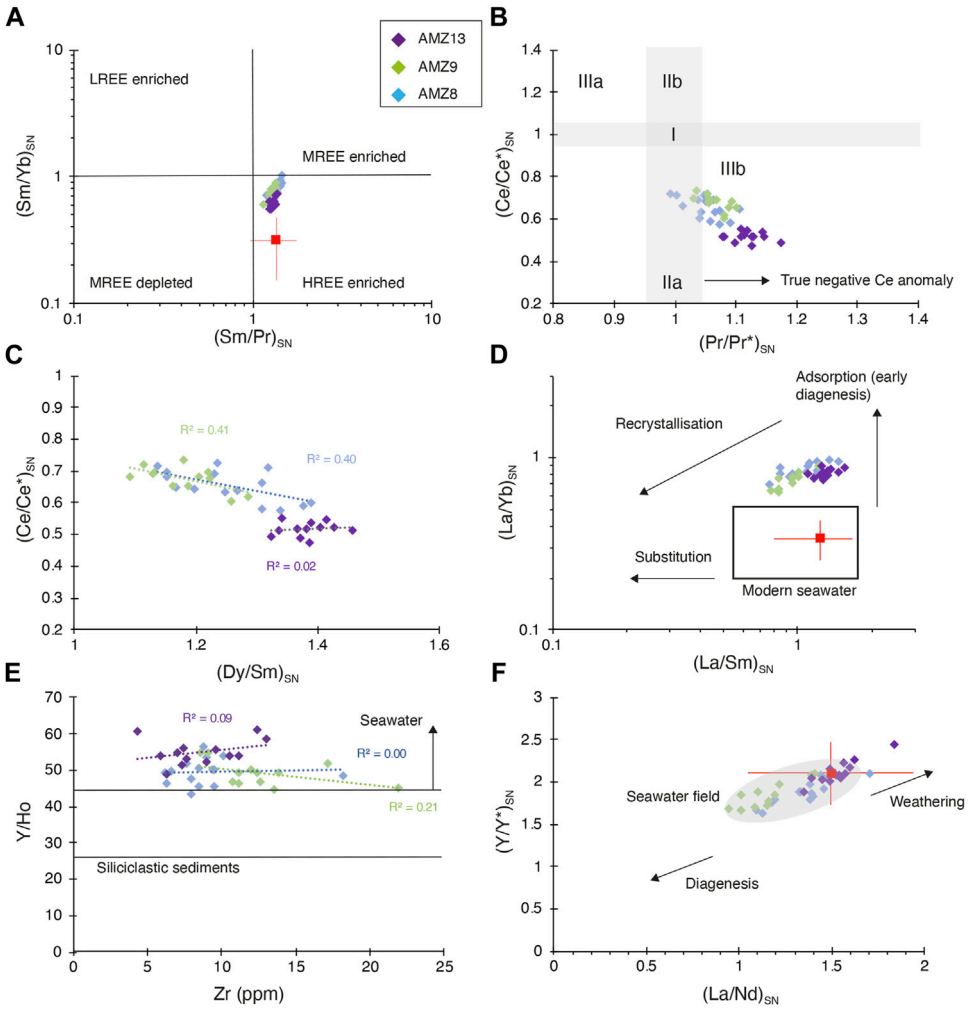

FIGURE 7
REEY cross-plots highlighting the effect of both depositional setting and diagenesis. Mean $REEY_{SN}$ value (n = 22, 1σ) of unaltered, Plio-Quaternay Namibian phosphorites is shown by the red square (Lumiste et al., 2019). **(A)** $(Sm/Yb)_{SN}$ vs. $(Sm/Pr)_{SN}$, after Garnit et al. (2012). Light (La to Nd), Middle (Sm to Dy), and Heavy (Ho to Lu) REE referred to as LREE, MREE, and HREE, respectively. **(B)** Ce anomaly vs. Pr anomaly, after Bau and Dulski (1996). Field **(I)** no La and Ce anomalies; Fields IIa and IIb: apparent negative and positive Ce caused by positive and negative La anomaly, respectively; Fields IIIa and IIIb: true positive and negative Ce anomaly, respectively. **(C)** Ce anomaly vs. $(Dy/Sm)_{SN}$, after Shields and Stille (2001). **(D)** $(La/Yb)_{SN}$ vs. $(La/Sm)_{SN}$, after Reynard et al. (1999). **(E)** Y/Ho vs. Zr, after Bolhar et al. (2004). **(F)** Y anomaly vs. $(La/Nd)_{SN}$, after Shields and Stille (2001). PAAS values are from Taylor and McLennan (1985).

(Figure 7E), which is above the typical seawater ratio of 44 (Bolhar et al., 2004). Such high Y/Ho values reflect the lower affinity of Y towards metal oxides in oxygenated seawater (Bau et al., 1997; Planavsky et al., 2010). The absence of mixing trend towards Y/Ho molar ratio of ~26, characterizing the terrestrial rocks (Bolhar et al., 2004), indicates that the CFA-hosted REEY concentrations are unlikely to be sourced from clay minerals or Fe–Mn oxyhydroxides during early diagenesis. Similarly, Y/Ho values do not correlate with Zr in the MHA CFA peloids (Figure 7E), suggesting no siliciclastic detrital influence on the REEY composition of CFA peloids. Finally, $(Y/Y^*)_{SN}$ and $(La/Nd)_{SN}$ ratios plot within the seawater field, with the exception of three peloids (Figure 7F). Y anomalies have average values of 1.85 ± 0.15, 1.84 ± 0.15, and 2.11 ± 0.14, while $(La/Nd)_{SN}$ average values are 1.32 ± 0.18, 1.14 ± 0.15, and 1.54 ± 0.12 for the AMZ8, AMZ9, and AMZ13 samples, respectively. Y anomaly and $(La/Nd)_{SN}$ values are expected to increase during weathering due to the lanthanide tetrad effect (Bau et al., 1996), resulting in the preferential retention of the more stable La, Gd, and Y elements. Also, diagenesis lowers the La content and reduces the Y anomaly (Shields and Stille, 2001), which is not observed in our samples.

In light of these considerations, we interpret the observed $REEY_{SN}$ distribution in the MHA CFA peloids to record a weak or 'early' diagenetic adsorption from oxic to suboxic, seawater-

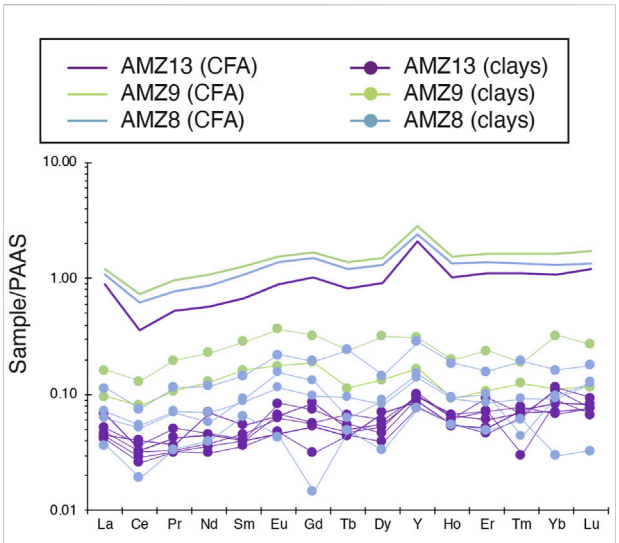

FIGURE 8
$REEY_{SN}$ patterns of Amizmiz samples from the Moroccan High Atlas. Data comparisons between CFA peloids (average values) and clay matrix. $REEY_{SN}$ patterns of clay minerals are not strongly different from those of CFA grains. However, values are, at least, ten times lower. PAAS values are from Taylor and McLennan (1985).

dominated pore fluids with a limited effect of detrital material. The absence of MREE enrichment precludes extensive or 'late' diagenetic recrystallization (Reynard et al., 1999) and influence of anoxic porewaters (Haley et al., 2004; Kocsis et al., 2009). The removal of non-tetrad REE is not shown by our dataset, which supports no post-depositional weathering influence. High hydrothermal activity, attributed to strong Eu_{SN} enrichment, is not recorded by the CFA grains. Thus, the $REEY_{SN}$ patterns mirror near-pristine marine composition, implying that post-depositional alterations on the U-Pb geochronometer were unlikely.

5.3.3 Trace element distribution in clay minerals

LA-ICP-MS analyses of the clay matrix were also conducted to decipher whether phyllosilicates could have strongly influenced the U-Pb chronometry (Supplementary Table S7). Detrital clay material usually has a flat PAAS-normalized REEY pattern with no anomaly diagnostic of marine environments (Tostevin et al., 2016). $REEY_{SN}$ patterns of the MHA clay minerals are similar to those of the CFA grains (Figure 8), although their $REEY_{SN}$ contents are much lower by up to ≤10-fold, implying that the clay matrix formed from seawater-dominated pore fluids. Alternatively, the presence of CFA crystallites in the matrix (Figures 3A–C, 4E,F) could have overprinted clay $REEY_{SN}$ patterns. Importantly, the U concentrations of clays average 3.11 ± 1.77 ppm (n = 12), which is radically smaller than those of CFA grains (49.35 ± 10.33 ppm, n = 40). The observed composition in clay minerals could result from lower adsorption rates and affinity for REEY and U from seawater relative to the phosphate minerals (Valsami-Jones et al., 1998; Trueman and Tuross, 2002; Moldoveanu and Papangelakis, 2012; Kunhikrishnan et al., 2022). Thus, if clay mineral-hosted uranium had contributed to the U-Pb date estimates, this influence would have been weak.

6 Understanding the U-Pb CFA dating

U-Pb ages of the MHA phosphorites, which are by far younger than the expected late Danian to early Thanetian biostratigraphic ages, do not obviously record phosphate precipitation at the water-sediment interface. Therefore, our studied samples were subjected to closer scrutiny. The loss of U decay products is unlikely as most of our U-Pb LA-ICP-MS data are aligned along robust discordias.

The petrographic, mineralogical, and geochemical screens reveal the presence of sepiolite/palygorskite clay minerals in close association with the phosphate material; both inside and outside, precipitated from high alkaline-saline seawater under hot arid climatic conditions, following either storm and bottom current wash-over transport to the inner platform or sea-level fall. The morphology of phosphate peloids, however, excludes the influence of significant hydrodynamic transport. The precise timing of clay formation after phosphogenesis remains uncertain, but would have occurred when the specific chemical conditions for sepiolite-palygorskite authigenesis were met. The depositional environment in the Amizmiz sequence becoming shallower during the late Paleocene to early Eocene, together with global warming events at that time (Zachos et al., 2001), could have been suitable for precipitation of sepiolite-palygorskite. Thus, the Mg-rich phyllosilicates in the late Danian-early Thanetian phosphorites would have crystallized from supersaturated interstitial conditions several million years (<5 Myr) after phosphate formation. High porosity in phosphate peloids (Mänd et al., 2018; Lumiste et al., 2019; Aubineau et al., 2022), could not have prevented circulation of fluids between CFA crystallites. Considering the lower amount of clays compared to CFA within the analyzed LA-ICP-MS volumes, together with low clay-hosted U contents, these Mg-rich phyllosilicates are, however, unlikely to influence the U-Pb dating. Overall, the reported U-Pb dates do not record the clay authigenesis.

REEY are usually released from organic and oxyhydroxide particulates through redox-driven organic matter remineralization and reductive dissolution of oxyhydroxides in sediments (Jarvis et al., 1994). REEY in porewaters may be either incorporated into the crystal lattice at the time of apatite precipitation or absorbed onto their surface sites during early diagenesis (Reynard et al., 1999). Rates of REEY uptake into bioapatite are presumably fast on geological timescales, $<10^5$ years (Trueman and Tuross, 2002; Kohn,

2008), which implies that the REEY composition of phosphate minerals mirrors that of the medium in which they precipitate within the next hundreds of thousands of years. As long as typical seawater-like $REEY_{SN}$ pattern is preserved, $REEY_{SN}$ patterns of phosphate minerals are therefore interpreted to reflect ambient seawater-dominated pore fluids during early diagenesis. In addition, REEY enrichments in phosphorites is time-independent (Figure 6; Reynard et al., 1999; Baioumy and Farouk, 2022) and controlled by the REEY composition of seawater, redox-controlled mechanisms during early diagenesis, burial, or post-depositional processes (McArthur and Walsh, 1985; Haley et al., 2004; Lécuyer et al., 2004; Kocsis et al., 2009).

Also, the $REEY_{SN}$ compositions of the MHA samples are strongly enriched by several orders of magnitude ($>10^6$) with respect to seawater, which may point to long-term interactions with seawater-dominated porewaters. Based on the REEY geochemistry from this study, adsorption mechanism would have been the dominant process of REEY uptake onto the MHA CFA crystallite surfaces, resulting in a slight fractionation of $(La/Yb)_{SN}$ ratios compared to seawater. The degree of adsorption may have controlled differences of REEY patterns and concentrations in phosphorites (Reynard et al., 1999), explaining the slight heterogeneity of MHA $REEY_{SN}$ patterns relative to trends observed for unaltered phosphorites of different ages. Combined to adsorption, diffusion of REEY takes place in phosphate biominerals as a consequence of the large surface to volume ratio of the µm-sized phosphate crystals (Millard and Hedges, 1996; Kohn, 2008). As we have shown, such tiny crystallites characterized the MHA phosphate peloids. Furthermore, diffusion models predict homogeneous REEY concentrations in phosphate minerals (Millard and Hedges, 1996; Kohn, 2008). There are no significant differences in REEY concentrations from the edge to the core of the MHA phosphate peloids, with the exception of one sample (Supplementary Table S6), which likely indicates the presence of open system diffusion and re-equilibration with seawater-dominated porewaters for extended intervals.

Because adsorption, desorption and diffusion processes affect the distribution of REEY on the crystallite surfaces, it is reasonable to assume that a wide range of less immobile elements (e.g., U) would have behaved similarly. Besides, the crystallographic position of U in sedimentary CFA is uncertain. U may be incorporated in the CFA lattice or adsorbed onto the crystallite surfaces (Jarvis et al., 1994). Combined, this raises questions on the effectiveness of the U-Pb chronometer to precisely deduce the age of sedimentary phosphate precipitation, especially where minute phosphate crystals are present. If the U-Pb chronometry represents ages of phosphate precipitation, the CFA crystallites should behave as a closed system over time, with U uptake limited to the time of CFA formation. However, our U-Pb dating and geochemical investigation suggest that trace elements uptake may have not been limited to the first hundreds of thousands of years.

Similarly, Lu-Hf dating of bioapatite have yielded robust but younger ages >30 Ma than the expected biostratigraphic depositional ages (Kocsis et al., 2010; Herwartz et al., 2011, 2013), which is thought to result from the specific apatite crystallite size facilitating adsorption, desorption and diffusion processes and thus long-term open system behavior (e.g., Herwartz et al., 2013). Open system behavior over a prolonged timescale would have caused a REE uptake over millions of years in fossils (Kocsis et al., 2010; Herwartz et al., 2011, 2013), perturbing the Lu-Hf system. Trueman and Tuross (2002) suggested that the rapid infilling of pore spaces and intercrystalline porosity by mineral authigenesis would probably prevent diffusion of elements at the crystallite surface of apatite minerals. In other words, closure of the inter- and intragranular porosity would have lowered the P-rich crystallites-porewater interactions during diagenesis, which, in turn, would have likely protected crystallite surfaces from further exchange. The inherent porous structures of CFA peloids (Mänd et al., 2018; Lumiste et al., 2019), together with the crumbly MHA phosphate rocks, denote that the clay authigenesis alone, occurring rapidly after phosphogenesis on the geological timescale, would have not been sufficient to decrease both the pore spaces and intercrystalline porosity in the MHA phosphorites. We, thus, hypothesized that the µm-sized MHA CFA crystallites would have had the ability to chemically re-equilibrate with ambient medium upon long-term interactions with seawater-dominated fluids.

7 Significance of U-Pb ages of sedimentary CFA

Radiometric U-Pb LA-ICP-MS dating of Phanerozoic phosphorites are scarce and not well unconstrained (Molnár et al., 2018; O'Sullivan et al., 2021), probably because sedimentary apatite group minerals may be subject to alteration that could lead to diagenetic addition and loss of U and radiogenic daughter isotopes (e.g., Balter et al., 2008; Romer, 2001).

Robust U-Pb dating associated with primary CFA grains and seawater-like $REEY_{SN}$ patterns in the MHA granular phosphorites are clearly unique data. While phosphate peloids rapidly form as little as few years after nucleation (Burnett et al., 1988), intense adsorption and diffusion processes would have significantly delayed the closed system behavior. Such considerations are particularly important because the MHA phosphate grains were continuously flushed by seawater-dominated fluids, which would have accounted for desorption of old bound U into the phosphorites as new U atoms from porewaters would have replaced the older ones. The 15–25 Myr time gap between biostratigraphic and chronological ages

corresponds to a long-term open system behavior that needs to be taken with caution when interpreting geochemical data.

To our knowledge, two geological events could have inhibited the phosphate-porewater interactions. First, occlusion of pore spaces and intercrystalline porosity by mineral precipitation combined with rock compaction, resulting in sediment lithification, may have helped to lock the U-Pb system. Overall, lithification partly depends on sedimentation rates that are often low in phosphogenesis zones, estimated for example to be <20 m/Myr in the Peru Margin (Burnett et al., 1988; Filippelli, 1997) and consistent with the estimated sedimentation rates for the Amizmiz phosphate series. Consequently, a low sedimentation rate would have possibly amplified the long-term open system behavior of the MHA CFA crystallites. Moreover, in northwest Africa, the first stage of shortening and uplift of the Atlas domain possibly occurred during the middle to late Eocene (Michard et al., 2008; Frizon de Lamotte et al., 2009), which is in good agreement with our U-Pb dates of 42.9 ± 1.3 Ma (AMZ8 and AMZ9) and 35.7 ± 2.8 Ma (AMZ13). Therefore, the U-Pb ages of CFA could have recorded the beginning of the Atlas uplift. This would have drained the basin, preserving the recorded open system interaction of seawater with the shallow water sediments before final disconnection from seawater. Both lithification and Atlas orogeny may also have concurrently occurred.

Regardless of the cause that led to CFA crystallites assuming a closed system behavior, the REEY compositions of the MHA CFA escaped overprinting by post-depositional processes after phosphate precipitation, indicating that the origin of interstitial pore fluids was unchanged. Oxic to suboxic seawater-dominated porewaters were predominant until the system was closed by either lithification or drainage associated with the Atlas orogeny. In spite of evidence for temporal occurrences of lagoonal to deltaic sedimentation in the aftermath of Thanetian in the MHA (El Bamiki et al., 2020), fluids with strong seawater characteristics would have continuously percolated to the underlying phosphate-rich sediments, until definitive continentalization during the middle to late Eocene orogenic uplift. If true, the inferred U-Pb ages might be pointing to the early stages of the Atlas orogeny, marked by the uplifting of sediments and permanent termination of the exposure of the MHA grains to seawater.

The sedimentary thickness corresponding to a minimum time lapse of 15 Myr between biostratigraphic and chronological ages can be approximately estimated in the Amizmiz sequence. With the available biostratigraphic data, it approximates at least 100 m but could be twice as thick, which implies extensive percolated fluids from seawater. In modern environments, the microbially influenced conversion of smectite to illite is possibly promoted by K-bearing seawater fluids percolating down to 700 m below the seafloor through terrigenous turbidites and mudstones (Kim et al., 2019). We, thus, propose that a shallow marine sediments platform on the eastern passive margin of the central Atlantic Ocean remained opened and in stable connection with oxygenated seawater for at least 15 Myr after the Paleogene phosphogenic events. In the Amizmiz carbonates and marls, these redox conditions of seawater are further supported by the presence of abundant *Thalassinoides* galleries that reflect burrow ventilation and oxygen uptake by animals (El Bamiki, 2020; El Bamiki et al., 2020).

8 Conclusion

This study does not support the application of U-Pb CFA dating to constrain the chronostratigrahy of sedimentary phosphate rock sequences. The data however suggest that when combined with geochemical screening of CFA grains and the surrounding matrix and cement composition, U-Pb dating of CFA grains can be used to reconstruct the geodynamic and redox evolution of seawater as well as shallow sediment porewater fluids, long after deposition. This is attributed to the fact that the intrinsic feature of the nm- to μm-sized crystallites of sedimentary apatite group minerals allows efficient adsorption and diffusion to take place. This behavior enables real-time recording of seawater-sediment history, long after deposition of the CFA minerals, the drawback being that past events are erased. Therefore, it is impossible to predict the exact seawater conditions under which the grains initially formed. Importantly, extensive or "late" diagenetic alteration is not required to explain the observed time gap. Nonetheless, important information can be retrieved, including the age of closed system behavior and thus of the processes responsible for it. Considering the low sedimentation rate in upwelling-related phosphogenic areas, a further question is whether U-Pb dating of sedimentary CFA peloids in non-upwelling, continental margin environments under high sedimentation rate (e.g., Ruttenberg and Berner, 1993), yields the expected stratigraphic age. Alternatively, larger CFA crystallite sizes should be targeted for U-Pb dating (Herwartz et al., 2013).

The open system behavior of μm CFA crystallites, as suggested by our results, limits the use of phosphorite-hosted REEY as paleoseawater proxies for paleoceanographic, taphonomic, and paleoenvironmental reconstructions. If sedimentary CFA behaves as closed system millions of years after precipitation, REEY will be inherited from diachronous seawater-connected fluids. Petrography, mineralogy, and trace element geochemistry have barely helped to decipher how long the open system behavior lasted in this study. In contrast, because the U-Pb geochronometer for CFA grains is shown to be useful in constraining the extent of U-Pb exchange in sedimentary phosphate-rich environments, it is proposed as a geodynamic and seawater-sediment porewater fluid chronometer capable of recording real-time events long after sediment deposition, as a function of system closure time.

Data availability statement

The original contributions presented in the study are included in the article/Supplementary Material, further inquiries can be directed to the corresponding author.

Author contributions

JA, FP, ECF, and MS contributed to conception and design of the study. JA, OM, FB, and MP were involved in the data acquisition. JA, FP, ECF, REB, FB, MP, and MS wrote the manuscript. REB and MS contributed to the fieldwork. All authors read and approved the submitted version.

Acknowledgments

We would like to thank the support of Mohammed VI Polytechnic University (UM6P), University of Montpellier (UM) (UM6P-UM specific agreement n°UM 190775 relating to the UM6P-UM/CNRS framework agreement n° UM 190759) and, OCP S.A. (OCP) (OCP-UM6P specific agreement n° 7 "Multi-scale distribution of minor and trace elements in Moroccan phosphate deposits" relating to the OCP-UM6P framework agreement in Sciences and Technology). Es-Said Jourani, former Director of OCP Geology, and Jamal Amalik, OCP Innovation, are warmly thanked for their constant help and support of collaborative projects between OCP, UM6P, and UM. We specially thank Paul Antonio (UM) for aiding in the construction of Tera-Wasserburg diagrams. Olivier Bruguier, Frédéric Fernandez, and Bernard Fraisse are thanked for their technical assistance during analytical works performed at, respectively, AETE, MEA, and RRXG platforms of UM. We deeply acknowledge Claude Laforest for the preparation of high-quality polished slab sections at IC2MP, University of Poitiers (UP). The authors specially thank Abderrazak El Albani and Alain Meunier for scientific support and Claude Fontaine for laboratory support at IC2MP (UP). The authors also thank financial support from the European Union (ERDF) and Région Nouvelle Aquitaine.

Conflict of interest

The authors declare that the research was conducted in the absence of any commercial or financial relationships that could be construed as a potential conflict of interest.

Publisher's note

All claims expressed in this article are solely those of the authors and do not necessarily represent those of their affiliated organizations, or those of the publisher, the editors and the reviewers. Any product that may be evaluated in this article, or claim that may be made by its manufacturer, is not guaranteed or endorsed by the publisher.

Supplementary material

The Supplementary Material for this article can be found online at: https://www.frontiersin.org/articles/10.3389/feart.2022.997008/full#supplementary-material

References

Ahmad, F., Baioumy, H., Farouk, S., Al-Kahtany, K., El-Sorogy, A., and Kirk, J. (2020). Geochemistry and stable isotopes of the upper Campanian–lower Maastrichtian phosphorite-bearing sequence, Central Jordan: Implications for their age, origin, and diagenesis. *Geol. J.* 55, 4453–4468. doi:10.1002/gj.3692

Akbulut, A., and Kadir, S. (2003). The Geology and origin of sepiolite, palygorskite and saponite in Neogene lacustrine sediments of the serinhisar-acipayam basin, denizli, SW Turkey. *Clays Clay Min.* 51, 279–292. doi:10.1346/CCMN.2003.0510304

Alibo, D. S., and Nozaki, Y. (1999). Rare earth elements in seawater: Particle association, shale-normalization, and Ce oxidation. *Geochimica Cosmochimica Acta* 63, 363–372. doi:10.1016/S0016-7037(98)00279-8

Altschuler, Z. S. (1980). "The geochemistry of trace metals in marine phosphorites: Part 1. Characteristics abundances and enrichment," in *Marine phosphorites*. Editor Y. K. Bentor (Oklahoma: SEPM). Special Publication no, 29.

Arning, E. T., Lückge, A., Breuer, C., Gussone, N., Birgel, D., and Peckmann, J. (2009). Genesis of phosphorite crusts off Peru. *Mar. Geol.* 262, 68–81. doi:10.1016/j.margeo.2009.03.006

Aubineau, J., Bankole, O. M., Baron, F., Grégoire, B., and El Albani, A. (2021). Authigenic kaolinite and sudoite in sandstones from the Paleoproterozoic Franceville sub-basin (Gabon). *Comptes Rendus Géoscience* 353, 209–226. doi:10.5802/crgeos.62

Aubineau, J., Parat, F., Elghali, A., Raji, O., Addou, A., Bonnet, C., et al. (2022). Highly variable content of fluorapatite-hosted CO_3^{2-} in the Upper Cretaceous/Paleogene phosphorites (Morocco) and implications for paleodepositional conditions. *Chem. Geol.* 597, 120818. doi:10.1016/j.chemgeo.2022.120818

Baioumy, H., and Farouk, S. (2022). The geochemical and economic significance of REE in the Upper Cretaceous-Eocene Tethyan phosphorites. *J. Afr. Earth Sci.* 194, 104635. doi:10.1016/j.jafrearsci.2022.104635

Balter, V., Blichert-Toft, J., Braga, J., Telouk, P., Thackeray, F., and Albarède, F. (2008). U–Pb dating of fossil enamel from the Swartkrans Pleistocene hominid site, South Africa. *Earth Planet. Sci. Lett.* 267, 236–246. doi:10.1016/j.epsl.2007.11.039

Bau, M., and Dulski, P. (1996). Distribution of yttrium and rare-earth elements in the Penge and kuruman iron-formations, transvaal Supergroup, South Africa. *Precambrian Res.* 79, 37–55. doi:10.1016/0301-9268(95)00087-9

Bau, M., Koschinsky, A., Dulski, P., and Hein, J. R. (1996). Comparison of the partitioning behaviours of yttrium, rare earth elements, and titanium between hydrogenetic marine ferromanganese crusts and seawater. *Geochimica Cosmochimica Acta* 60, 1709–1725. doi:10.1016/0016-7037(96)00063-4

Bau, M., Möller, P., and Dulski, P. (1997). Yttrium and lanthanides in eastern Mediterranean seawater and their fractionation during redox-cycling. *Mar. Chem.* 56, 123–131. doi:10.1016/S0304-4203(96)00091-6

Bolhar, R., Kamber, B. S., Moorbath, S., Fedo, C. M., and Whitehouse, M. J. (2004). Characterisation of early Archaean chemical sediments by trace element signatures. *Earth Planet. Sci. Lett.* 222, 43–60. doi:10.1016/j.epsl.2004.02.016

Boujo, A. (1976). Contribution à l'étude géologique du gisement de phosphate crétacé-éocène des Ganntour (Maroc Occidental). *Sci. Géologiques, Bull. mémoires* 43. Available at: https://www.persee.fr/doc/sgeol_0302-2684_1976_mon_43_1 (Accessed April 21, 2022).

Brindley, G. W., and Brown, G. (1980). *Crystal structure of clay minerals and their X-ray identification*. London: Mineralogical Society.

Burnett, W. C., Baker, K. B., Chin, P. A., McCabe, W., and Ditchburn, R. (1988). Uranium-series and AMS ^{14}C studies of modern phosphatic pellets from Peru shelf muds. *Mar. Geol.* 80, 215–230. doi:10.1016/0025-3227(88)90091-6

Chellaï, E. H., Marzoqi, M., Pascal, A., and Mouflih, M. (1995). "Stratigraphy and evolution of upper cretaceous-palaeogene sedimentary systems in the marrakesh high Atlas (Morocco)," in *Comptes Rendus-Académie des Sciences de Paris Série II A*, 321, 745–752.

Chew, D. M., Petrus, J. A., and Kamber, B. S. (2014). U–Pb LA–ICPMS dating using accessory mineral standards with variable common Pb. *Chem. Geol.* 363, 185–199. doi:10.1016/j.chemgeo.2013.11.006

Chien, S. H., and Black, C. A. (1976). Free energy of formation of carbonate apatites in some phosphate rocks. *Soil Sci. Soc. Am. J.* 40, 234–239. doi:10.2136/sssaj1976.03615995004000020015x

Cochrane, R., Spikings, R. A., Chew, D., Wotzlaw, J.-F., Chiaradia, M., Tyrrell, S., et al. (2014). High temperature (>350°C) thermochronology and mechanisms of Pb loss in apatite. *Geochimica Cosmochimica Acta* 127, 39–56. doi:10.1016/j.gca.2013.11.028

Comodi, P., and Liu, Y. (2000). CO_3 substitution in apatite: further insight from new crystal-chemical data of kesekere (Uganda) apatite. *Eur. J. Mineral.* 12, 965–974. doi:10.1127/ejm/12/5/0965

Cosmidis, J., Benzerara, K., Gheerbrant, E., Estève, I., Bouya, B., and Amaghzaz, M. (2013). Nanometer-scale characterization of exceptionally preserved bacterial fossils in Paleocene phosphorites from Ouled Abdoun (Morocco). *Geobiology* 11, 139–153. doi:10.1111/gbi.12022

Daoudi, L., Knidiri, A., and Rhouta, B. (2009). Structure, properties and genesis of Moroccan palygorskite. *Orient. J. Chem.* 25, 855–862.

Daoudi, L. (2004). Palygorskite in the uppermost cretaceous–eocene rocks from marrakech high Atlas, Morocco. *J. Afr. Earth Sci.* 39, 353–358. doi:10.1016/j.jafrearsci.2004.07.033

De Baar, H. J. W., Brewer, P. G., and Bacon, M. P. (1985). Anomalies in rare earth distributions in seawater: Gd and Tb. *Geochimica Cosmochimica Acta* 49, 1961–1969. doi:10.1016/0016-7037(85)90090-0

Diaz, J., Ingall, E., Benitez-Nelson, C., Paterson, D., de Jonge, M. D., McNulty, I., et al. (2008). Marine polyphosphate: A key player in geologic phosphorus sequestration. *Science* 320, 652–655. doi:10.1126/science.1151751

El Bamiki, R. (2020). *Étude géologique des occurrences phosphatées du Haut-Atlas marocain : Compréhension des contrôles géologiques sur l'accumulation du phosphate*.

El Bamiki, R., Séranne, M., Chellaï, E. H., Merzeraud, G., Marzoqi, M., and Melinte-Dobrinescu, M. C. (2020). The Moroccan High Atlas phosphate-rich sediments: Unraveling the accumulation and differentiation processes. *Sediment. Geol.* 403, 105655. doi:10.1016/j.sedgeo.2020.105655

Ellouz, N., Patriat, M., Gaulier, J.-M., Bouatmani, R., and Sabounji, S. (2003). From rifting to Alpine inversion: Mesozoic and Cenozoic subsidence history of some Moroccan basins. *Sediment. Geol.* 156, 185–212. doi:10.1016/S0037-0738(02)00288-9

Farmer, V. C. (1974). *The infrared spectra of minerals*. London: The mineralogical Society.

Fassett, J. E., Heaman, L. M., and Simonetti, A. (2011). Direct U-Pb dating of cretaceous and Paleocene dinosaur bones, san juan basin, New Mexico. *Geology* 39, 159–162. doi:10.1130/G31466.1

Filippelli, G. M. (1997). Controls on phosphorus concentration and accumulation in oceanic sediments. *Mar. Geol.* 139, 231–240. doi:10.1016/S0025-3227(96)00113-2

Filippelli, G. M. (2011). Phosphate rock formation and marine phosphorus geochemistry: The deep time perspective. *Chemosphere* 84, 759–766. doi:10.1016/j.chemosphere.2011.02.019

Föllmi, K. (1996). The phosphorus cycle, phosphogenesis and marine phosphate-rich deposits. *Earth-Science Rev.* 40, 55–124. doi:10.1016/0012-8252(95)00049-6

Frizon de Lamotte, D. F., Leturmy, P., Missenard, Y., Khomsi, S., Ruiz, G., Saddiqi, O., et al. (2009). Mesozoic and Cenozoic vertical movements in the Atlas system (Algeria, Morocco, Tunisia): An overview. *Tectonophysics* 475, 9–28. doi:10.1016/j.tecto.2008.10.024

Frizon de Lamotte, D., Zizi, M., Missenard, Y., Hafid, M., El Azzouzi, M., Maury, R. C., et al. (2008). "The Atlas system," in *Continental evolution: The Geology of Morocco: Structure, stratigraphy, and tectonics of the africa-atlantic-mediterranean triple junction lecture notes in earth sciences*. Editors A. Michard, O. Saddiqi, A. Chalouan, and D. Frizon de Lamotte (Berlin, Heidelberg: Springer), 133–202. doi:10.1007/978-3-540-77076-3_4

Garnit, H., Bouhlel, S., Barca, D., and Chtara, C. (2012). Application of LA-ICP-MS to sedimentary phosphatic particles from Tunisian phosphorite deposits: Insights from trace elements and REE into paleo-depositional environments. *Geochemistry* 72, 127–139. doi:10.1016/j.chemer.2012.02.001

Gheerbrant, E., Cappetta, H., Feist, M., Jaeger, J.-J., Sudre, J. V.-L., and Sigé, B. (1993). Succession of faunas of vertebrates from the Upper Paleocene and the Early Eocene in the Ouarzazate basin (Morocco). Geological context, biostratigraphical and paleogeographical scope. *Newsl. Stratigr.* 28, 33–58. doi:10.1127/nos/28/1993/33

Glenn, C. R., Arthur, M. A., Yeh, H., and Burnett, W. C. (1988). Carbon isotopic composition and lattice-bound carbonate of Peru-Chile margin phosphorites. *Mar. Geol.* 80, 287–307. doi:10.1016/0025-3227(88)90094-1

Glenn, C. R., Föllmi, K., Riggs, S. R., Baturin, G. N., Grimm, K. A., Trappe, J., et al. (1994). Phosphorus and phosphorites: Sedimentology and environments of formation. *Eclogae Geol. Helv.* 87, 747–788. 0012-9402194/030747-42.

Greene, S., Heaman, L. M., DuFrane, S. A., Williamson, T., and Currie, P. J. (2018). Introducing a geochemical screen to identify geologically meaningful U-Pb dates in fossil teeth. *Chem. Geol.* 493, 1–15. doi:10.1016/j.chemgeo.2018.04.022

Haley, B. A., Klinkhammer, G. P., and McManus, J. (2004). Rare earth elements in pore waters of marine sediments. *Geochimica Cosmochimica Acta* 68, 1265–1279. doi:10.1016/j.gca.2003.09.012

Herwartz, D., Münker, C., Tütken, T., Hoffmann, J. E., Wittke, A., and Barbier, B. (2013). Lu–Hf isotope systematics of fossil biogenic apatite and their effects on geochronology. *Geochimica Cosmochimica Acta* 101, 328–343. doi:10.1016/j.gca.2012.09.049

Herwartz, D., Tütken, T., Münker, C., Jochum, K. P., Stoll, B., and Sander, P. M. (2011). Timescales and mechanisms of REE and Hf uptake in fossil bones. *Geochimica Cosmochimica Acta* 75, 82–105. doi:10.1016/j.gca.2010.09.036

Hollard, H., Choubert, G., Bronner, G., Marchand, J., and Sougy, J. (1985). *Carte géologique du Maroc. Échelle 1/1 000 000*.

Jahnke, R. A. (1984). The synthesis and solubility of carbonate fluorapatite. *Am. J. Sci.* 284, 58–78. doi:10.2475/ajs.284.1.58

Jarvis, I., Burnett, W. C., Nathan, Y., Almbaydin, F. S. M., Attia, A. K. M., Castro, L. N., et al. (1994). Phosphorite geochemistry: state-of-the-art and environmental concerns. *Eclogae Geol. Helvetiae* 87, 643–700.

Jasinski, S. M. (2020). *Phosphate rock*.

Jolivet, M., Lebatard, A. E., Reyss, J. L., Bourlès, D., Mackaye, H. T., Lihoreau, F., et al. (2008). Can fossil bones and teeth be dated using fission track analysis? *Chem. Geol.* 247, 81–99. doi:10.1016/j.chemgeo.2007.10.009

Kadir, S., Eren, M., İrkeç, T., Erkoyun, H., Külah, T., Önalgil, N., et al. (2017). An approach to genesis of sepiolite and palygorskite in lacustrine sediments of the lower pliocene sakarya and porsuk formations in the Sivrihisar and yunusemre-bi̇çer regions (Eskişehi̇r), Turkey. *clays clay Min.* 65, 310–328. doi:10.1346/CCMN.2017.064067

Kadir, S., Erkoyun, H., Eren, M., Huggett, J., and Önalgil, N. (2016). Mineralogy, geochemistry, and genesis of sepiolite and palygorskite in Neogene lacustrine sediments, eskişehir province, west central anatolia, Turkey. *Clays Clay Min.* 64, 145–166. doi:10.1346/CCMN.2016.0640206

Kidder, D. L., Krishnaswamy, R., and Mapes, R. H. (2003). Elemental mobility in phosphatic shales during concretion growth and implications for provenance analysis. *Chem. Geol.* 198, 335–353. doi:10.1016/s0009-2541(03)00036-6

Kim, J., Dong, H., Yang, K., Park, H., Elliott, W. C., Spivack, A., et al. (2019). Naturally occurring, microbially induced smectite-to-illite reaction. *Geology* 47, 535–539. doi:10.1130/G46122.1

Kim, K.-H., Byrne, R. H., and Lee, J. H. (1991). Gadolinium behavior in seawater: a molecular basis for gadolinium anomalies. *Mar. Chem.* 36, 107–120. doi:10.1016/s0304-4203(09)90057-3

Knidiri, A., Daoudi, L., El Ouahabi, M., Rhouta, B., Rocha, F., and Fagel, N. (2014). Palaeogeographic controls on palygorskite occurrence in maastrichtian-palaeogene sediments of the western high Atlas and Meseta basins (Morocco). *Clay Min.* 49, 595–608. doi:10.1180/claymin.2014.049.4.08

Kocsis, L., Gheerbrant, E., Mouflih, M., Cappetta, H., Ulianov, A., Chiaradia, M., et al. (2016). Gradual changes in upwelled seawater conditions (redox, pH) from the late Cretaceous through early Paleogene at the northwest coast of Africa: Negative

Ce anomaly trend recorded in fossil bio-apatite. *Chem. Geol.* 421, 44–54. doi:10.1016/j.chemgeo.2015.12.001

Kocsis, L., Gheerbrant, E., Mouflih, M., Cappetta, H., Yans, J., and Amaghzaz, M. (2014). Comprehensive stable isotope investigation of marine biogenic apatite from the late Cretaceous–early Eocene phosphate series of Morocco. *Palaeogeogr. Palaeoclimatol. Palaeoecol.* 394, 74–88. doi:10.1016/j.palaeo.2013.11.002

Kocsis, L., Ősi, A., Vennemann, T., Trueman, C. N., and Palmer, M. R. (2009). Geochemical study of vertebrate fossils from the Upper Cretaceous (Santonian) Csehbánya Formation (Hungary): Evidence for a freshwater habitat of mosasaurs and pycnodont fish. *Palaeogeogr. Palaeoclimatol. Palaeoecol.* 280, 532–542. doi:10.1016/j.palaeo.2009.07.009

Kocsis, L., Trueman, C. N., and Palmer, M. R. (2010). Protracted diagenetic alteration of REE contents in fossil bioapatites: Direct evidence from Lu–Hf isotope systematics. *Geochimica Cosmochimica Acta* 74, 6077–6092. doi:10.1016/j.gca.2010.08.007

Koenig, A. E., Lucas, S. G., Neymark, L. A., Heckert, A. B., Sullivan, R. M., Jasinski, S. E., et al. (2012). Direct U-Pb dating of cretaceous and Paleocene dinosaur bones, san juan basin, New Mexico: COMMENT. *Geology* 40, e262. doi:10.1130/G32154C.1

Kohn, M. J. (2008). Models of diffusion-limited uptake of trace elements in fossils and rates of fossilization. *Geochimica Cosmochimica Acta* 72, 3758–3770. doi:10.1016/j.gca.2008.05.045

Krajewski, K. P., Van Cappellen, P., Trichet, J., Kuhn, O., Lucas, J., Martin-Algarra, A., et al. (1994). Biological processes and apatite formation in sedimentary environments. *Eclogae Geol. Helv.* 87, 701–745. doi:10.5169/SEALS-167475

Kunhikrishnan, A., Rahman, Md. A., Lamb, D., Bolan, N. S., Saggar, S., Surapaneni, A., et al. (2022). Rare earth elements (REE) for the removal and recovery of phosphorus: A review. *Chemosphere* 286, 131661. doi:10.1016/j.chemosphere.2021.131661

Lécuyer, C., Reynard, B., and Grandjean, P. (2004). Rare earth element evolution of Phanerozoic seawater recorded in biogenic apatites. *Chem. Geol.* 204, 63–102. doi:10.1016/j.chemgeo.2003.11.003

LeGeros, P. G., Trautz, O. R., LeGeros, J. P., Klein, E., and Shirra, W. P. (1967). Apatite crystallites: Effects of carbonate on morphology. *Science* 155, 1409–1411. doi:10.1126/science.155.3768.1409

Lumiste, K., Mänd, K., Bailey, J., Paiste, P., Lang, L., Lepland, A., et al. (2019). REE+Y uptake and diagenesis in Recent sedimentary apatites. *Chem. Geol.* 525, 268–281. doi:10.1016/j.chemgeo.2019.07.034

Madejová, J., Balan, E., and Petit, S. (2011). "Application of vibrational spectroscopy to the characterization of phyllosilicates and other industrial minerals," in *Advances in the characterization of industrial minerals*. Editor G. E. Christidis (London, United Kingdom: European Mineralogical Union), 171–226. doi:10.1180/EMU-notes.9.6

Mänd, K., Kirsimäe, K., Lepland, A., Crosby, C. H., Bailey, J. V., Konhauser, K. O., et al. (2018). Authigenesis of biomorphic apatite particles from Benguela upwelling zone sediments off Namibia: The role of organic matter in sedimentary apatite nucleation and growth. *Geobiology* 16, 640–658. doi:10.1111/gbi.12309

McArthur, J. M. (1978). Systematic variations in the contents of Na, Sr, CO_3 and SO_4 in marine carbonate-fluorapatite and their relation to weathering. *Chem. Geol.* 21, 89–112. doi:10.1016/0009-2541(78)90008-6

McArthur, J. M., and Walsh, J. N. (1985). Rare-earth geochemistry of phosphorites. *Chem. Geol.* 47, 191–220. doi:10.1016/0009-2541(84)90126-8

McClellan, G. H. (1980). Mineralogy of carbonate fluorapatites. *J. Geol. Soc. Lond.* 137, 675–681. doi:10.1144/gsjgs.137.6.0675

McClellan, G. H., and Van Kauwenbergh, S. J. (1991). Mineralogical and chemical variation of francolites with geological time. *J. Geol. Soc. Lond.* 148, 809–812. doi:10.1144/gsjgs.148.5.0809

McDowell, F. W., McIntosh, W. C., and Farley, K. A. (2005). A precise ^{40}Ar–^{39}Ar reference age for the Durango apatite (U–Th)/He and fission-track dating standard. *Chem. Geol.* 214, 249–263. doi:10.1016/j.chemgeo.2004.10.002

Meunier, A. (2005). *Clays*. Berlin ; New York: Springer.

Michard, A., Saddiqi, O., Chalouan, A., and Frizon de Lamotte, D. (2008). *Continental evolution: The Geology of Morocco*. Berlin, Heidelberg: Springer.

Middleton, G. V., Church, M. J., Coniglio, M., Hardie, L. A., and Longstaffe, F. J. (2003). *Encyclopedia of sediments and sedimentary rocks*. Boston: Springer Netherlands.

Millard, A. R., and Hedges, R. E. (1996). A diffusion-adsorption model of uranium uptake by archaeological bone. *Geochimica Cosmochimica Acta* 60, 2139–2152. doi:10.1016/0016-7037(96)00050-6

Moldoveanu, G. A., and Papangelakis, V. G. (2012). Recovery of rare earth elements adsorbed on clay minerals: I. Desorption mechanism. *Hydrometallurgy* 117–118, 71–78. doi:10.1016/j.hydromet.2012.02.007

Molnár, Z., Kiss, G. B., Dunkl, I., Czuppon, G., Zaccarini, F., and Dódony, I. (2018). Geochemical characteristics of triassic and cretaceous phosphorite horizons from the transdanubian mountain range (western Hungary): genetic implications. *Mineral. Mag.* 82, S147–S171. doi:10.1180/minmag.2017.081.103

Morad, S., and Felitsyn, S. (2001). Identification of primary Ce-anomaly signatures in fossil biogenic apatite: implication for the cambrian oceanic anoxia and phosphogenesis. *Sediment. Geol.* 143, 259–264. doi:10.1016/S0037-0738(01)00093-8

Nathan, Y. (1984). "The mineralogy and geochemistry of phosphorites," in *Phosphate minerals*. Editors J. O. Nriagu and P. B. Moore (Berlin, Heidelberg: Springer-Verlag), 275–291.

O'Sullivan, G. J., Daly, J. S., Murray, J., Ó'Gogáin, A., Chew, D. M., Drakou, F., et al. (2021). Uranium–lead phosphate chronostratigraphy: A proof of concept from the mid-carboniferous boundary. *Sediment. Geol.* 422, 105961. doi:10.1016/j.sedgeo.2021.105961

Pearce, N. J., Perkins, W. T., Westgate, J. A., Gorton, M. P., Jackson, S. E., Neal, C. R., et al. (1997). A compilation of new and published major and trace element data for NIST SRM 610 and NIST SRM 612 glass reference materials. *Geostand. Geoanal. Res.* 21, 115–144. doi:10.1111/j.1751-908x.1997.tb00538.x

Planavsky, N. J., Bekker, A., Rouxel, O. J., Kamber, B., Hofmann, A., Knudsen, A., et al. (2010). Rare earth element and yttrium compositions of Archean and Paleoproterozoic Fe formations revisited: New perspectives on the significance and mechanisms of deposition. *Geochimica Cosmochimica Acta* 74, 6387–6405. doi:10.1016/j.gca.2010.07.021

Pochon, A., Poujol, M., Gloaguen, E., Branquet, Y., Cagnard, F., Gumiaux, C., et al. (2016). U-Pb LA-ICP-MS dating of apatite in mafic rocks: Evidence for a major magmatic event at the Devonian-Carboniferous boundary in the Armorican Massif (France). *Am. Mineralogist* 101, 2430–2442. doi:10.2138/am-2016-5736

Pufahl, P. K., and Grimm, K. A. (2003). Coated phosphate grains: Proxy for physical, chemical, and ecological changes in seawater. *Geol.* 31, 801–804. doi:10.1130/G19658.1

Pufahl, P. K., and Groat, L. A. (2017). Sedimentary and igneous phosphate deposits: Formation and exploration: An invited paper. *Econ. Geol.* 112, 483–516. doi:10.2113/econgeo.112.3.483

Reynard, B., Lécuyer, C., and Grandjean, P. (1999). Crystal-chemical controls on rare-earth element concentrations in fossil biogenic apatites and implications for paleoenvironmental reconstructions. *Chem. Geol.* 155, 233–241. doi:10.1016/S0009-2541(98)00169-7

Rochín-Bañaga, H., Davis, D. W., and Schwennicke, T. (2021). First U-Pb dating of fossilized soft tissue using a new approach to paleontological chronometry. *Geology* 49, 1027–1031. doi:10.1130/G48386.1

Romer, R. L. (2001). Isotopically heterogeneous initial Pb and continuous 222Rn loss in fossils: The U-Pb systematics of Brachiosaurus brancai. *Geochimica Cosmochimica Acta* 65, 4201–4213. doi:10.1016/s0016-7037(01)00716-5

Ruttenberg, K. C., and Berner, R. A. (1993). Authigenic apatite formation and burial in sediments from non-upwelling, continental margin environments. *Geochimica Cosmochimica Acta* 57, 991–1007. doi:10.1016/0016-7037(93)90035-U

Ruttenberg, K. C. (2003). "The global phosphorus cycle," in *Treatise on geochemistry*. Editor W. H. Schlesinger (Elsevier), 8, 585–643.

Sano, Y., and Terada, K. (1999). Direct ion microprobe U–Pb dating of fossil tooth of a Permian shark. *Earth Planet. Sci. Lett.* 174, 75–80. doi:10.1016/s0012-821x(99)00253-8

Sano, Y., Terada, K., Ly, C. V., and Park, E. J. (2006). Ion microprobe U-Pb dating of a dinosaur tooth. *Geochem. J.* 40, 171–179. doi:10.2343/geochemj.40.171

Schoene, B., and Bowring, S. A. (2006). U–Pb systematics of the McClure mountain syenite: thermochronological constraints on the age of the ^{40}Ar/^{39}Ar standard MMhb. *Contrib. Mineral. Petrol.* 151, 615–630. Article number: 615. doi:10.1007/s00410-006-0077-4

Schuffert, J. D., Kastner, M., Emanuele, G., and Jahnke, R. A. (1990). Carbonate-ion substitution in francolite: A new equation. *Geochimica Cosmochimica Acta* 54, 2323–2328. doi:10.1016/0016-7037(90)90058-S

Schulz, H. N., and Schulz, H. D. (2005). Large sulfur bacteria and the formation of phosphorite. *Science* 307, 416–418. doi:10.1126/science.1103096

Shields, G., and Stille, P. (2001). Diagenetic constraints on the use of cerium anomalies as palaeoseawater redox proxies: an isotopic and REE study of cambrian phosphorites. *Chem. Geol.* 175, 29–48. doi:10.1016/S0009-2541(00)00362-4

Singer, A., and Galan, E. (1984). *Palygorskite-Sepiolite: Occurrences, genesis and uses*. Amsterdam: Elsevier.

Soares, G. G., Van Kranendonk, M. J., Belousova, E., and Thomson, S. (2019). Phosphogenesis in the immediate aftermath of the great oxidation event: Evidence from the turee creek group, western Australia. *Precambrian Res.* 320, 193–212. doi:10.1016/j.precamres.2018.10.017

Stacey, J. S., and Kramers, J. D. (1975). Approximation of terrestrial lead isotope evolution by a two-stage model. *Earth Planet. Sci. Lett.* 26, 207–221. doi:10.1016/0012-821X(75)90088-6

Suárez, M., García-Romero, E., Sánchez Del Río, M., Martinetto, P., and Dooryhée, E. (2007). The effect of the octahedral cations on the dimensions of the palygorskite cell. *Clay Min.* 42, 287–297. doi:10.1180/claymin.2007.042.3.02

Suárez, M., and García-Romero, E. (2013). Sepiolite–palygorskite: A continuous polysomatic series. *Clays Clay Min.* 61, 461–472. doi:10.1346/CCMN.2013.0610505

Tabuce, R., Adnet, S., Cappetta, H., Noubhani, A., and Quillevere, F. (2005). Aznag (Ouarzazate basin, Morocco), a new African middle Eocene (Lutetian) vertebrate-bearing locality with selachians and mammals. *Bull. Société Géologique Fr.* 176, 381–400. doi:10.2113/176.4.381

Taylor, S. R., and McLennan, S. M. (1985). *The continental crust: Its composition and evolution*. Oxford: Blackwell Scientific Puplications.

Tostevin, R., Shields, G. A., Tarbuck, G. M., He, T., Clarkson, M. O., and Wood, R. A. (2016). Effective use of cerium anomalies as a redox proxy in carbonate-dominated marine settings. *Chem. Geol.* 438, 146–162. doi:10.1016/j.chemgeo.2016.06.027

Trueman, C. N., and Tuross, N. (2002). Trace elements in recent and fossil bone apatite. *Rev. Mineralogy Geochem.* 48, 489–521. doi:10.2138/rmg.2002.48.13

Valetich, M., Zivak, D., Spandler, C., Degeling, H., and Grigorescu, M. (2022). REE enrichment of phosphorites: An example of the Cambrian Georgina Basin of Australia. *Chem. Geol.* 588, 120654. doi:10.1016/j.chemgeo.2021.120654

Valsami-Jones, E., Ragnarsdottir, K. V., Putnis, A., Bosbach, D., Kemp, A. J., and Cressey, G. (1998). The dissolution of apatite in the presence of aqueous metal cations at pH 2–7. *Chem. Geol.* 151, 215–233. doi:10.1016/S0009-2541(98)00081-3

Vermeesch, P. (2018). IsoplotR: A free and open toolbox for geochronology. *Geosci. Front.* 9, 1479–1493. doi:10.1016/j.gsf.2018.04.001

Weaver, C. E., and Beck, K. C. (1977). Miocene of the S.E. United states: A model for chemical sedimentation in a peri-marine environment. *Sediment. Geol.* 17, IX–234. doi:10.1016/0037-0738(77)90062-8

Wilson, M. J. (2013). "Rock-Forming Miner" in *Sheet Silicates: Clay minerals*. second ed. (London: The Geological Society of London), 3C.

Yang, H., Zhao, Z., Xia, Y., and Xiao, J. (2021). REY enrichment mechanisms in the early Cambrian phosphorite from South China. *Sediment. Geol.* 426, 106041. doi:10.1016/j.sedgeo.2021.106041

Yans, J., Amaghzaz, M., Bouya, B., Cappetta, H., Iacumin, P., Kocsis, L., et al. (2014). First carbon isotope chemostratigraphy of the Ouled Abdoun phosphate Basin, Morocco; implications for dating and evolution of earliest African placental mammals. *Gondwana Res.* 25, 257–269. doi:10.1016/j.gr.2013.04.004

Zachos, J., Pagani, M., Sloan, L., Thomas, E., and Billups, K. (2001). Trends, rhythms, and aberrations in global climate 65 Ma to present. *Science* 292, 686–693. doi:10.1126/science.1059412